## IN THE UNITED STATES PATENT AND TRADEMARK OFFICE

| | | | |
|---|---|---|---|
| Applicant | : | Jackson Streeter et al. | Group Art Unit 3739 |
| Appl. No. | : | 10/764,986 | |
| Filed | : | January 26, 2004 | |
| For | : | LOW LEVEL LIGHT THERAPY FOR THE ENHANCEMENT OF NEUROLOGICAL FUNCTION | |
| Examiner | : | Henry M. Johnson III | |

## DECLARATION OF LUIS DE TABOADA PURSUANT TO 37 C.F.R. § 1.132

Commissioner for Patents
P.O. Box 1450
Alexandria, VA  22313-1450

Dear Sir:

I, Luis De Taboada, declare as follows:

1.      I am a co-inventor of the claimed subject matter of the above-captioned patent application.

2.      I have reviewed the above-captioned patent application, including the specification and figures, the claims as originally filed, and the pending claims as amended in the "Amendment and Response to May 31, 2007 Office Action" submitted herewith.  I have also reviewed the May 31, 2007 Office Action in the above-captioned patent application, and the prior art reference cited therein, namely, PCT Publication No. WO 99/62599 to Oron ("Oron").

3.      At page 6, lines 21-27, Oron discloses invasive phototherapy experiments that were performed on rats by cutting an incision in the scalp to expose the skull and attaching a laser source to the parietal bone in the skull.  Oron further discloses that an energy density of 8 mW per square centimeter reached the brain tissue of the rats.  At page 7, lines 7-9, Oron further discloses phototherapy experiments that were performed on white mice by irradiating through the

skin that covers the skull. Oron further discloses that an energy density of 5 mW per square centimeter reached the brain tissue of the mice.

4.     A rat or mouse brain is typically only about 10 to 12 millimeters in diameter, so no portion of the rat brain is at a depth of approximately 2 centimeters below the dura of the brain. In addition, due at least in part to the drastically different size of a human brain versus a rat or mouse brain, it is not obvious that irradiation of the surface of a rat or mouse brain would have a corresponding effect if performed on a human brain. Persons skilled in the art of phototherapy would understand the disclosure of Oron as not disclosing or suggesting non-invasively irradiating a portion of a brain with light having a power density at least about 0.01 mW per square centimeter at a depth of approximately 2 centimeters below the dura.

5.     At page 8, lines 4-13, Oron also discloses measurements of the penetration of laser irradiation through a fresh human skull to illustrate the transmittance of light through the skull wall. Oron discloses that the beam diameter of the laser was dispersed from 2 millimeters externally to the skull to 3.5 centimeters in the skull cavity and had a power density of 3 mW per square centimeter after penetration through a skull wall having a thickness of about 8 millimeters. Oron is silent regarding the transmission of light through human brain tissue. Oron is also silent regarding the irradiation of the brain with light at a point approximately 2 centimeters below the dura. Persons skilled in the art of phototherapy would understand from the disclosure of Oron that Oron does not disclose or suggest irradiating a portion of the brain approximately 2 centimeters below the dura with light having a power density at least about 0.01 mW per square centimeter.

6.     Transmission of light through a material is described by the Beer-Lambert Law, which can be expressed as $I(L) = (1 - R_F) * I_0 * e^{-\mu_t L}$, where $I_0$ is the input intensity, $L$ is the linear distance from the input point to the measured point, $I(L)$ is the intensity of light after propagating through a thickness $L$ of the material, $R_F$ is the relative mean refractive index of the material, and $\mu_t$ is the total attenuation coefficient. The total attenuation coefficient can be expressed as: $\mu_t = \mu_a + (1 - g)\mu_s$, where $\mu_a$ is the absorption coefficient, $\mu_s$ is the scattering coefficient, and $g$ is the scattering anisotropy parameter. The quantity $(1-g)\mu_s$ is referred to as the reduced scattering coefficient $\mu'_s$.

7.      The published literature on the optical properties of brain tissue at the time of Oron stated that the absorption coefficient $\mu_a$ of brain tissue was about 0.090 cm$^{-1}$, and the reduced scattering coefficient $\mu'_s$ of brain tissue was about 8.2 cm$^{-1}$. (*See, e.g.*, Pogue et al., *"Comparison of imaging geometries for diffuse optical tomography of tissue,"* Optics Express, Vol. 4, No. 8, 12 April 1999, pages 270-286; Bevilacqua et al., *"In vivo local determination of tissue optical properties: applications to human brain,"* Applied Optics, Vol. 38, No. 22, 1 August 1999, pages 4939-4950; Firbank et al., *"A Theoretical Study of the Signal Contribution of Regions of the Adult Head to Near-Infrared Spectroscopy Studies of Visual Evoked Responses,"* Neuroimage, Vol. 8, 1998, pages 69-78; each of which is included in the attached Exhibit A.) Assuming that the relative mean refractive index of brain tissue is equal to zero (thereby providing the maximum transmitted intensity), the Beer-Lambert Law would be used by persons skilled in the art to determine that application of a power density of 8 mW/cm$^2$ at the surface of the human brain would yield about 5 x 10$^{-7}$ mW/cm$^2$ at a depth of 2 centimeters. Thus, persons skilled in the art would not expect that application of the power densities disclosed by Oron would result in a power density of at least about 0.01 mW/cm$^2$ at a depth of 2 centimeters below the dura.

8.      In addition, using these accepted prior art values for the absorption and transmission coefficients for brain tissue, persons skilled in the art would expect that in order to get a power density of at least about 0.01 mW/cm$^2$ at a depth of 2 centimeters below the dura, a power density of about 159 W/cm$^2$ would be needed at the surface of the brain. Persons skilled in the art would recognize that this power density would cause significant damage of the patient's brain and would not be practical for treatment.

9.      Despite the teachings of the prior art that the transmission of light through brain tissue was too low to make phototherapy of the brain practical, the above-captioned patent application describes a technique of enhancing neurological function in a patient by noninvasively irradiating the patient's brain. To provide support for our contention that the actual transmission of light through brain tissue is higher than was expected from the prior art references, I took part in a pair of separate studies in which the transmission of radiation through a cadaver human skull and through a cadaver human brain was measured. In the skull transmission study (V.V. Lychagov *et al.*, *"Experimental study of NIR transmittance of the human skull,"* Complex Dynamics and Fluctuations in Biomedical Photonics III, ed. by V.V.

Tuchin, Proc. of SPIE Vol. 6085, 6085T (2006), attached herewith as Exhibit B), an input beam having a wavelength of 810 nm, a power density of about 68 mW per square centimeter, and a beam diameter of about 30 millimeters was applied to the shaved skin of the skulls of 20 cadavers at five regions with various thicknesses. Figure 2 of Exhibit B illustrates that the transmittance of the light varied from 0.5% to 5%, depending on the thickness of the irradiated portion of the skull. We performed an independent measurement (unpublished) of the transmission of 808-nm light with a power density of 424 mW per square centimeter applied to a cadaver human skull (including the shaved skin) having an average thickness of about 11 millimeters, and calculated the overall transmittance of the skull tissues to be about 2%, which agrees well with the results of Exhibit B.

10.    In the brain transmission study (unpublished), measurements showed that for an input beam having a wavelength of 808 nm, a power density of 10 mW per square centimeter applied directly to the dura, and a beam diameter $(1/e^2)$ of 30 millimeters at the dura, the power density at a depth of 1.5 centimeters from the dura was 0.148 mW per square centimeter, and the power density at a depth of 2.5 centimeters from the dura was 0.010 mW per square centimeter.

11.    I hereby declare that all statements made herein of my own knowledge are true, and that all statements made upon information and belief are believed to be true; and further, that these statements were made with the knowledge that willful, false statements and the like so made are punishable by fine or imprisonment, or both under Section 1001, Title 18 of the United States Code, and that willful, false statements may jeopardize the validity of the application or any patent issuing thereon.

Dated: __10/5/2007__          By: _____
                                      Luis De Taboada

4322824
092607

-4-

# EXHIBIT A

# Comparison of imaging geometries for diffuse optical tomography of tissue

**Brian W. Pogue, Troy O. McBride, Ulf L. Osterberg and Keith D. Paulsen**

*Thayer School of Engineering, Dartmouth College, Hanover NH*
*pogue@dartmouth.edu*

**Abstract:** Images produced in six different geometries with diffuse optical tomography simulations of tissue have been compared using a finite element-based algorithm with iterative refinement provided by the Newton-Raphson approach. The source-detector arrangements studied include (i) fan-beam tomography, (ii) full reflectance and transmittance tomography, as well as (iii) sub-surface imaging, where each of these three were examined in a circular and a flat slab geometry. The algorithm can provide quantitatively accurate results for all of the tomographic geometries investigated under certain circumstances. For example, quantitatively accurate results occur with sub-surface imaging only when the object to be imaged is fully contained within the diffuse projections. In general the diffuse projections must sample all regions around the target to be characterized in order for the algorithm to recover quantitatively accurate results. Not only is it important to sample the whole space, but maximal angular sampling is required for optimal image reconstruction. Geometries which do not maximize the possible sampling angles cause more noise artifact in the reconstructed images. Preliminary simulations using a mesh of the human brain confirm that optimal images are produced from circularly symmetric source-detector distributions, but that quantitatively accurate images can be reconstructed even with a sub-surface imaging, although spatial resolution is modest.

## References and links

1. M. Cope, and D. T. Delpy, "System for long-term measurement of cerebral blood and tissue oxygenation on newborn infants by near-infrared transillumination," Med. Biol. Eng. Comp. **26**, 289-294 (1988).
2. B. Chance, Q. Luo, S. Nioka, D. C. Alsop and J. A. Detre, "Optical investigations of physiology: a study of intrinsic and extrinsic biomedical contrast," Phil. Trans. R. Soc. Lond. B **352**, 707-716 (1997).
3. M. A. Franceschini, K. T. Moesta, S. Fantini, G. Gaida, E. Gratton, H. Jess, H., W. W. Mantulin, M. Seeber, P. Schlag and M. Kaschke, "Frequency-domain techniques enhance optical mammography: initial clinical results," Proc. Nat. Acad. Sci USA **94**, 6468-73 (1997).
4. S. R. Arridge and M. Schweiger, "Sensitivity to prior knowledge in optical tomographic resconstruction," Proc. SPIE **2389**, 378-388 (1995).
5. V. Ntziachristos, M. O,Leary, B. Chance and A. G. Yodh, "Coregistration of images from diffusive wave with other imaging modalities to enhance specificity," in OSA TOPS on Advances in Optical Imaging and Photon Migration II. (OSA publications, Orlando, FL, 1996).
6. J. Chang, H. Graber, P. Koo, R. Aronson, S. S. Barbour, R. L. Barbour, "Optical imaging of anatomical maps derived from magnetic resonance images using time independent optical sources," IEEE Trans. Med. Imag. **16**, 68-77 (1997).
7. B. W. Pogue and K.D. Paulsen, "High resolution near infrared tomographic imaging simulations of rat cranium using apriori MRI structural information," Opt. Lett. **23**, 1716-8 (1998).
8. C. L. Hutchinson, J.R. Lakowicz, and E.M. Sevick-Muraca, "Fluorescence lifetime-based sensing in tissues: a computational study," Biophys. J. **68**, 1574-1582 (1995).
9. J. Chang, H.L. Graber, and R.L. Barbour, "Luminescence optical tomography of dense scattering media," J. Opt. Soc. Am. A **14**, 288-99 (1998).
10. S. R. Arridge, "Forward and inverse problems in time-resolved infrared imaging," in Medical Optical Tomography: Functional Imaging and Monitoring, Ed. G. Muller, (SPIE Optical Eng. Press, Bellingham, WA, 1993) pp. 35-64.

11. D. Boas, "A fundamental limitation of linearized algorithms for diffuse optical tomography," Opt. Express 1, 404-413 (1997). (http://epubs.osa.org/oearchive/source/2831.htm)
12. H. Jiang, K. D. Paulsen, U. L. Osterberg and M. S. Patterson, "Frequency-domain optical image reconstruction in turbid media: an experimental study of single-target detectability," Appl. Opt. 36, 52-63 (1997).
13. H. Jiang, K. D. Paulsen, U. L. Osterberg, and M. S. Patterson, "Frequency-domain optical image reconstruction for breast imaging: initial evaluation in multi-target tissue-like phantoms," Med. Phys. 25, 183-193 (1997).
14. B. W. Pogue, M. Testorf, U. L. Osterberg and K. D. Paulsen, "Instrumentation and design of a frequency-domain diffuse optical tomography imager for breast cancer detection," Opt. Express 1, 391-403 (1997). (http://epubs.osa.org/oearchive/source/2827.htm)
15. B. W. Pogue, T. O. McBride, J. Prewitt, U. L. Osterberg, and K. D. Paulsen, "Spatially variant regularization improves diffuse optical tomography," Appl. Opt. 38, (in press) 1999.
16. T. O. McBride, B. W. Pogue, E. Gerety, S. Poplack, U. L. Osterberg, and K. D. Paulsen, "Spectroscopic diffuse optical tomography for quantitatively assessing hemoglobin concentration and oxygenation in tissue," (submitted, 1999), .
17. M. S. Patterson, B. Chance and B. C. Wilson, "Time resolved reflectance and transmittances for the non-invasive measurement of tissue optical properties," Appl. Opt. 28, 2331-2336 (1989).
18. S. R. Arridge, M. Cope and D. T. Delpy, "The theoretical basis for the determination of optical pathlengths in tissue: temporal and frequency analysis," Phys. Med. Biol. 37, 1531-1560 (1992).
19. A. H. Gandjbakhche, V. Chernomordik, R.F. Bonner, J. C. Hebden, R. Nossal, "Use of time-dependent contrast functions to discriminate between the scattering and absorption properties of abnormal regions hidden within a tissue-like phantom," Proc. SPIE 2979, 211-225 (1997).
20. J. A. Moon, R. Mahon, M. D. Duncan and J. Reintjes, "Resolution limits for imaging through turbid media with diffuse light," Opt. Lett. 18, 1591-1593 (1993).
21. A. H. Gandjbakhche, R. Nossal and R. F. Bonner, "Resolution limits for optical transillumination of abnormalities deeply embedded in tissues," Med. Phys. 21, 185-91 (1994).
22. D. A. Boas, M. A. O'Leary, B. Chance and A. G. Yodh, "Detection and characterization of optical inhomogeneities with diffuse photon density waves: a signal-to-noise analysis," Appl. Opt. 36, 75-92 (1997).
23. H. Jess, H. Erdl, T. Moesta, S. Fantini, M. A. Francecshini, E. Gratton and M. Kaschke, "Intensity modulated breast imaging: Technology and clinical pilot study results," Adv. in Optical Imaging and Photon Migration. (OSA publications, Orlando, FL, 1996).
24. S. Fantini, O. Schutz, J. Edler, M. A. Franceschini, S. Heywang-Krbrunner, L. Gotz and H. Siebold, "Performance of N-Images and spectral features in frequency-domain optical mammography," SPIE Technical Abstract Digest. (SPIE Press, San Jose, CA, 1999).
25. Y. Painchaud, A. Mailloux, E. Harvey, S. Verrault, J. Frechette, C. Gilbert, M. L. Vernon and P. Beaudry, "Multi-port time-domain laser mammography: results on solid phantoms and volunteers," SPIE BiOS Technical Abstract Digest. (SPIE Press, San Jose, CA, 1999).
26. J. P. Van Houten, D. A. Benaron, S. Spilman and D. K. Stevenson, "Imaging brain injury using time-resolved near infrared light scanning," Pediat. Res. 39, 470-6 (1996).
27. M. R. Stankovic, A. Fujii, D. Maulik and D. Boas, "Optical monitoring of cerebral hemodynamics and oxygenation in the neonatal piglet," J. Matern-Fetal Inves. 8, 71-8 (1998).
28. A. Siegel, J. Marota, J. Mandeville, B. Rosen, and D. Boas, "Diffuse optical tomography of rat brain function," in SPIE Technical Abstract Digest. (SPIE Press, San Jose, CA, 1999).
29. S. Fantini, S. Walker, M. A. Franceschini, M. Kaschke, P. M. Schlag and K. T. Moesta, "Assessment of the size, position, and optical properties of breast tumors in vivo by noninvasive optical methods," Appl. Opt. 37, 1982-89 (1998).
30. V. Quaresima, S. J. Matcher and M. Ferrari, "Identification and quantification of intrinsic optical contrast for near-infrared mammography," Photochem. Photobiol. 67, 4-14 (1998).
31. X. Li, J. Culver, J., T. Durduran, B. Chance, A. G. Yodh and D. N. Pattanayak, "Diffraction tomography with diffuse-photon density waves: clinical studies and background subtraction," in Advances in Optical Imaging and Photon Migration. (OSA publications, Orlando, FL, 1993).
32. S. B. Colak, D. G. Papaioannou, G. W. t'Hooft, M. B. van der Mark, H. Schomberg, J. C. J. Paasschens, J. B. M. Melissen and N. A. A. J. van Asten, "Tomographic image reconstruction from optical projections in light-diffusing media," Appl. Opt. 36, 180-213 (1997).
33. S. R. Arridge and M. Schweiger, "Gradient-based optimisation scheme for optical tomography," Opt. Exp. 2, 212-226 (1998). (http://epubs.osa.org/oearchive/source/4014.htm)
34. B. J. Tromberg, O. Coquoz, J. B. Fishkin, T. Pham, E. R. Anderson, J. Butler, M. Cahn, J. D. Gross, V. Venugopalan and D. Pham, "Non-invasive measurements of breast tissue optical properties using frequency-domain photon migration," Phil. Trans. R. Soc. Lond. B. 352, 661-668 (1997).
35. S. R. Arridge and M. Schweiger, "Inverse methods for optical tomography," in Information Processing in Medical Imaging (Springer-Verlag, Flagstaff, AZ, 1993).
36. K. D. Paulsen and H. Jiang "Spatially varying optical property reconstruction using a finite element diffusion equation approximation," Med. Phys. 22, 691-701 (1995).
37. S. R. Arridge and M. Schweiger, "Image reconstruction in optical tomography," Phil. Trans. R. Soc. Lond. B. 352, 717-726 (1997).
38. A. Neumaier, "Solving ill-conditioned and singular linear systems: a tutorial on regularization," SIAM Rev. 40, 636-666 (1998).

39. T. J. Yorkey, J. G. Webster and W. J. Tompkins, "Comparing reconstruction algorithms for electrical impedance tomography," IEEE Trans. Biomed. Eng. 34, 843-852 (1987).

40. B. W. Pogue, T. O. McBride, C. Nwaigwe, U. L. Osterberg, J. F. Dunn, K. D. Paulsen, "Near-infrared diffuse tomography with apriori MRI structural information: testing a hybrid image reconstruction methodology with functional imaging of the rat cranium," Proc. SPIE 3597 (in press), (1999).

## 1. Introduction

Diffuse Optical Tomography (DOT) imaging of tissue is emerging as a viable method for non-invasively determining hemoglobin concentration, hemoglobin oxygen saturation, cytochromes, lipids and water in vivo on a centimeter spatial scale. In the past decade, promising applications have emerged in areas such as neonatal and adult cerebral monitoring [1, 2] and breast cancer diagnosis [3]. In addition, DOT may be even more promising when combined with traditional imaging methods [4-7] or when coupled to exogenous contrast agents to monitor tissue function, either through fluorescence or absorption based imaging [2, 8, 9]. One of the limitations in this field of research has been that the rapid advances in technological instrumentation have eclipsed the development of accurate image reconstruction algorithms for diffuse tomography. In this study we focus on one particularly useful image reconstruction algorithm, and apply it in several different imaging configurations in order to evaluate how the source-detector-tissue geometry affects the resulting image.

The use of an appropriate reconstruction algorithm is important because the inverse problem for DOT is inherently ill-posed, and in many cases is ill-conditioned [10], so that standard linear approaches provide limited resolution and contrast inaccuracy [11]. Several iterative reconstruction methods have been tested, and in particular, the Newton-Raphson approach has been shown to provide quantitatively accurate images of the absorption coefficient in a circular tomographic geometry [12-16]. This approach has been developed to characterize breast tumor optical properties in order to diagnose changes in hemoglobin concentration and oxygen saturation of normal and malignant tissues, and is currently being used in our clinical prototype imager.
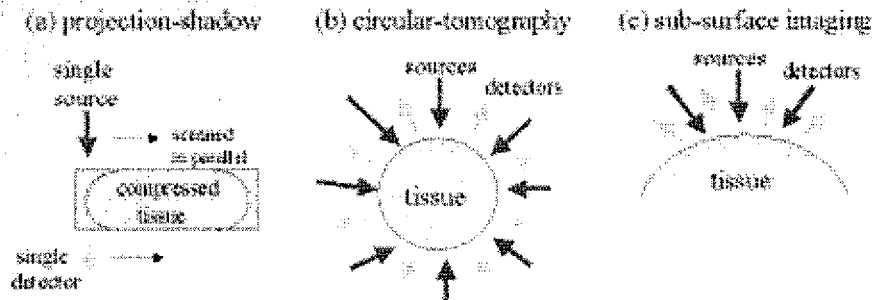


Fig. 1. Schematic of three typical source-detector geometries used in diffuse optical tomography applications. The projection-shadow geometry (a) is used in several optical mammography scanners [3, 23-25], while the circular-tomography geometry (b) is used for both breast and brain imaging [16, 26], as is the sub-surface imaging geometry (c) [2, 27, 28].

There has been considerable study of the type of measurements needed to provide optimal sensitivity in separating the scattering and absorption coefficients in tissue [17-19]. There has also been considerable study of the resolution limits of diffuse tomography [20-22]; however, in general the optimal data types and the resoluton limits are functions of the reconstruction algorithm used to retrieve the images and the source-detector arrangement. Resolution limits calculated from forward solutions may not apply to inversion algorithms which preserve the non-linearity between the internal optical properties of interest and the measured projections at the boundaries. Similarly there has been little investigation of the

geometry and how its boundaries affect the imaging process. As a practical matter, it is quite important to assess the effects that boundaries and source-detector configurations have on the image reconstruction in order to design prototype medical systems. These design considerations are ideally assessed through computer simulations to avoid costly and wasteful construction of clinical prototype systems which may have inherent design flaws. With this goal in mind, we assess geometries which to date represent the most common configurations used for near-infrared imaging and spectroscopy.
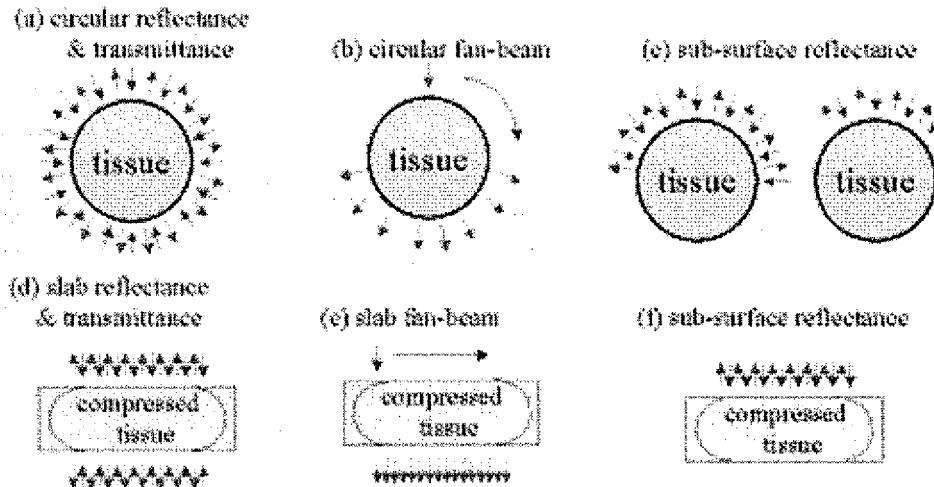


Fig. 2. Geometries used in this study are shown, where the outward arrows indicate detector locations and the inward arrows denote source locations. The geometries include (a) circular reflectance and transmittance imaging which uses circular symmetry for sampling angles (b) circular fan-beam imaging (where the source-detector array is rotated around the tissue), (c) sub-surface tomography which only uses a sub-set of projections from the surface of the tissue, (d) flat slab reflectance and transmittance imaging using maximal sampling from both surfaces, (e) flat slab fan-beam which does not use any reflectance data, and (e) sub-surface imaging with a flat upper surface. Together these six geometries, in various forms, define the possible configurations for imaging tissue with DOT.

The geometries chosen for many laboratory and clinical near-infrared imaging studies fall into three general catagories, which are delineated here as (a) projection-shadow, (b) circular-tomography and (c) subsurface imaging, as shown in Fig. 1. Each of these geometries is being used in clinical investigations for imaging either breast or brain tissues with near-infrared light; yet, there has been little comparison of how the source-detector array geometry will affects the quality of the optical measurements and resulting image. It should be noted that the projection-shadow geometry is generally used for traditional x-ray film style images, where there is no inversion of the data to compute tomographic images [3], and that this geometry does not lend itself to tomographic reconstruction. However, even with this restriction, Fantini et al. have been able to retrieve quantitative optical properties from breast tumors using the assumption that the tumor is roughly spherically shaped [29], and this procedure can be even more accurate when multiple projections and multiple wavelengths are incorporated into the analysis [24]. Similarly, Quaresima et al. have used this geometry to measure the spectral signature of breast tissue [30]. A variant of this geometry, which exploits a single source location and the angular projections to multiple detectors, has been employed by Li et al. [31] to produce backprojection images of breast tissue. Circular tomography has been used successfully in our own studies of hemoglobin based imaging [15, 16] which is being developed for breast cancer diagnosis [32], as well as in work of other investigators for cerebral imaging [26, 33].

In this study, the same DOT image reconstruction algorithm is used to examine: (a) circular full reflectance and transmittance tomography (b) circular fan-beam tomography, (c) sub-surface imaging under a curved boundary, (d) flat slab reflectance and transmittance tomography, (e) flat slab fan-beam tomography, and (f) sub-surface imaging below a flat surface, as shown in Fig. 2. The goal of these tests is to examine the influences of (i) the tissue geometry and (ii) the source-detector configuration upon the recovered image accuracy and quality, and to determine the optimal data collection strategy for characterizing tissue optical properties with this algorithm. The flat slab geometry (Fig. 2 (d) to (f)) is well suited for breast imaging since it provides a configuration similar to x-ray mammography, but it is not clear how the image quality will compare to the more symmetric sampling provided by the circular geometries (Fig. 2 (a) to (c)). We also compare a fan-beam orientation of the detectors where measurements are only recorded on the opposite side to the source (Fig. 2 (b) & (e)), with the full set of projections from all points equally spaced around the tissue (Fig. 2 (a) & (d)). The former orientation is technologically easier to implement because all measurement intensities are within the same range of detector sensitivity, so that parallel implementation is more easily facilitated. However, it is not obvious how this decrease in data affects the resulting optical property distribution, as compared to the full reflectance and transmittance sampling. Finally, subsurface tomography is examined since this is a geometry which is being widely used for near-infrared tomography of brain and breast tissues [2, 28, 34].

## 2. Theory & Computational Methods

The theoretical details of diffuse optical tomography have been described by several authors, and some good overviews are included in references [35-37]. Forward calculations of diffuse light in tissue can be used to simulate experimental measurements of heterogeneous tissue, and by matching calculated measurements to these simulated experimental measurements an image of the optical properties can be recovered. Since frequency-domain light measurements are used in this work, the frequency-domain diffusion equation is solved with a finite element method. The general form of this equation is:

$$\nabla \cdot D(r)\nabla \Phi(r,\omega) - [\mu_a(r) + i(\omega / c)]\Phi(r,\omega) = S_0(r,\omega)$$

(1)

which describes optical fluence rate $\Phi(r,\omega)$ at position r, and frequency $\omega$, given the distribution of absorption coefficient, $\mu_a(r)$ and diffusion coefficient $D(r)$, where c is the speed of light in the medium, and $S_0(r,\omega)$ is the optical source. The diffusion coefficient is usually defined as $D = [3(\mu_s' + \mu_a)]^{-1}$, where $\mu_s'$ is the transport scattering coefficient of the medium. This equation is solved with Type III (Robin) boundary condition on a finite element mesh, where all exterior elements are subject to:

$$\Phi(\xi) + k\nabla\Phi(\xi,\omega) \cdot \hat{n} = 0$$

(2)

where $\xi$ is the position on the boundary, $\hat{n}$ is the unit vector normal to the boundary, and k is a calibration constant which has been determined empirically by matching the forward calculations to well controlled experiments [36]. From this solution, we calculate a set of optical measurements, $\phi_i^0$, which in this case are phase shift at frequency, $\omega$, and the logarithm of the signal amplitude. While the solution to equation (1) is straightforward given the distribution of $\mu_a$ and $\mu_s'$, recovering the image distribution of $\mu_a$ and $\mu_s'$ requires an iterative solution, since equation (1) cannot be directly solved for these values, in part because $\Phi(r,\omega)$ is not known inside the tissue, but only at the discrete points (detector locations) on the boundary.

The Newon-Raphson iterative method for finding the solution of $\mu_a$ and $\mu_s'$ starts by solving for the minimum of the functional

$$\chi(\mu) = (\phi^C - \phi^O)^T (\phi^C - \phi^O) + \lambda F(\mu)$$

(3)

where we use $\mu$ to represent both $\mu_a$ and $\mu_s'$ as the set of coefficients, and $F(\mu)$ is an arbitrary functional which smooths the solution to reduce the ill-posed nature of the eventual matrix inversion [38]. Minimizing (3) by taking the derivative and setting it equal to zero, followed by expansion of the solution in a Taylor's series [39], leads to,

$$0 = (\phi^C - \phi^O)^T J + \Delta\mu(J^T J + \lambda I) + ...$$

(4)

where the elements of $J$ are given by $\partial\phi_i / \partial\mu_k$, for observation i, at each pixel position k. In this derivation, the higher order derivatives of $\phi$ are assumed to be negligible, and $F(\mu)$ is chosen to result in the classical Tikhonov regularized formulation [38]. Finally the iterative solution becomes,

$$\Delta\mu = (\phi^C - \phi^O)^T J [J^T J + \lambda I]^{-1}$$

(5)

where $\Delta\mu$ is the update for the current estimate of $\mu$. The values of $\phi^C$ and $J$ are calculated using the current estimate of $\mu$. In practice we have found that the regularization parameter can be varied between iterations for improved reconstruction, and can be varied spatially to compensate for some geometrical artifacts induced during the reconstruction process [15].

In the following simulations, the forward and inverse calculations have been carried out with a finite element solution which has been tested extensively in previous papers [ The simulated measurements were calculated on the same meshes that were used for the reconstructions and 1% random gaussian-distributed noise was added to both the real and imaginary components of the measurements in order to simulate true source-detector noise. All reconstructions were carried out with the same regularization parameter, and 5 iterations have been used in each case. Each iteration requires approximately 1.5 minutes on a 200 MHz desktop computer running Windows NT. In all the reconstructed images shown in this paper, the dimensions of the field are shown in millimeters on the x and y axes of the figure.

## 3. Results

### 3.1 Imaging Fields with a Single Localized Target

A series of forward and inverse simulations have been completed for each geometry shown in Figure 2. The overall goal has been to maintain a uniform test between geometries and determine those geometries which introduce significant artifacts into the reconstruction by the nature of the boundaries and source-detector configuration. There are an infinite number of possible tests which could be used in each of these geometries, but we have chosen to begin with a physiologically relevant contrast in a tumor sized target. In all cases the background optical properties were fixed at $\mu_a = 0.01$ mm$^{-1}$ and $\mu_s' = 1.0$ mm$^{-1}$, and a simulated target within the field has been included with a radius of 10 mm and optical properties of $\mu_a = 0.02$ mm$^{-1}$ and $\mu_s' = 1.0$ mm$^{-1}$. In each geometry the target is moved around to positions within the imaging field which have different levels of symmetry, potentially affecting the resulting image qualtity.

### 3.1.1 Circular Reflectance and Transmittance Imaging

A circular mesh was used with 221 nodes in the coarse calculation of the Jacobian and matrix inversion as shown in equation (5), and 425 nodes in the fine mesh were used for solution of equation (1). A circularly symmetric configuration of 16 sources and 16 detectors was used in the solution, providing a data set of 256 projections, as shown in Fig. 2 (a). The field was 86 mm in diameter, with the sources and detectors spaced symmetrically around the periphery, with one every 11.25 degrees alternating between source and detector. The test target was moved to different radial positions between the center and the edge of the field to

examine the quality of the reconstructions which are presented in Fig. 3. Because this simulation has circular symmetry, no other target locations are needed to characterize the image field.
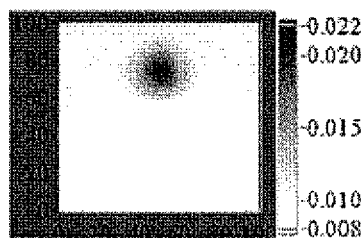


Fig. 3. Reconstructed set of images (video sequence) of the test target at different vertical positions within the circular mesh, using source-detector geometry in Fig. 2 (a) with a circularly symmetric distribution of 16 source and 16 detectors for reflectance and transmittance imaging. The color bar on the right is in absorption coefficient units of mm$^{-1}$.

### 3.1.2 Circular Fan-Beam Imaging

This orientation of source and detectors is shown in Fig 2(b), where for each source location, 8 detectors were used on the opposite side of the phantom. Then the source and locations of the 8 detectors are rotated around the phantom to 16 different sets of projections through the phantom, resulting in 128 measurements of phase shift and signal amplitude. The spacing of field and source-detectors was otherwise identical to Fig. 3. This geometry has the experimental advantage that the signal intensity at all 8 detectors is within an order of magnitude in variation, so that large changes in the dynamic range of the detectors is not encountered. This data set can be considered as a sub-set of the data available in the previous case of full reflectance and transmittance with the near-source detectors removed. The location of the test target was varied in the object field between the center and the top edge. Again, since the sources and detectors are located in circularly symmetric orientations, this set of target locations is sufficient to characterize the entire image field for this size and shape of object, as shown in Fig. 4.
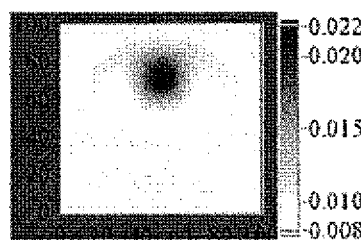


Fig. 4. Reconstructed set of images (video sequence) showing the test target at different vertical positions within the circular mesh, using the fan beam geometry with 16 sources transmitting to 8 detectors. The color bar on the right is in absorption coefficient units of mm$^{-1}$.

### 3.1.3 Sub-surface Imaging — Curved Boundary

Near-infrared imaging is confounded by the high attenuation of the light in tissue, such that in practice, it is often not possible to detect light reliably through tissue samples thicker than 10 cm. Also, the instrumentation for imaging through tissue less than 5-6 cm can be much simpler, more robust and less expensive than for thicker tissues [28]. For this reason, many investigators have focused on sub-surface imaging applications where the sources and detectors are located on the same tissue surface and are arranged to probe the interior of the tissue. This sub-surface tomography can be performed on a curved tissue such as a neonate or adult head and female breast. These tissues are well simulated with a finite element

solution assuming that the boundary curvature is known and can be input into a finite element mesh. If the light does not sample deeply into the tissue, the tissue boundary can be approximated by a simple circular mesh which has a matching radius of curvature. In the next series of simulations, this sub-surface imaging method has been investigated using the same circular mesh as above, but with only the source and detector locations on the upper region of the mesh activated. Both situations illustrated in Fig. 2 (c) were examined including: 8 sources-8 detectors (8x8) and 4 sources-4 detectors (4x4). The imaging field is symmetric about the center of the source-detector array, so that the image quality is adequately assessed by translating the test object vertically down from the upper surface, as shown in Fig. 5.
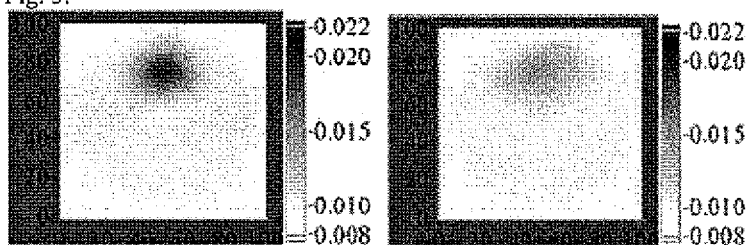


Fig. 5. Reconstructed set of images of the test target within a circular mesh using the sub-surface orientation with (a) 8 sources and 8 detectors in an arc, and (b) 4 sources and 4 detectors in a smaller arc on the surface (as shown in Fig. 2(c)). Color bar at right is in absorption coefficient units of mm$^{-1}$.

### 3.1.4 Slab Reflectance and Transmittance Imaging

The slab geometry mimics x-ray mammography and minimizing the thickness of tissue that must be imaged, potentially allowing the use of less sensitive, but more stable, solid state detectors. Light signals from the tissue can be recorded from both the upper surface near the source, as well as transmitted through the slab. This geometry is referred to here as slab reflectance and transmittance imaging, and is examined in the same set of simulations as the circular geometry described in the previous sections. One major difference from the circular geometry is the lack of symmetry, so that the response of the imaging field will likely vary with both vertical and horizontal position. Thus, in order to fully characterize the image plane, the test object has been translated along three lines: vertically through the center, horizontally through the center, as well as horizontally along the upper surface, as shown in Fig. 6. In the slab mesh, 260 nodes were used in the coarse calculation of the Jacobian in equation (5) and 380 nodes were used in the fine mesh solution of equation (1). The source detector arrangement was as shown in Fig. 2(d), with 5 mm between each source and detector.
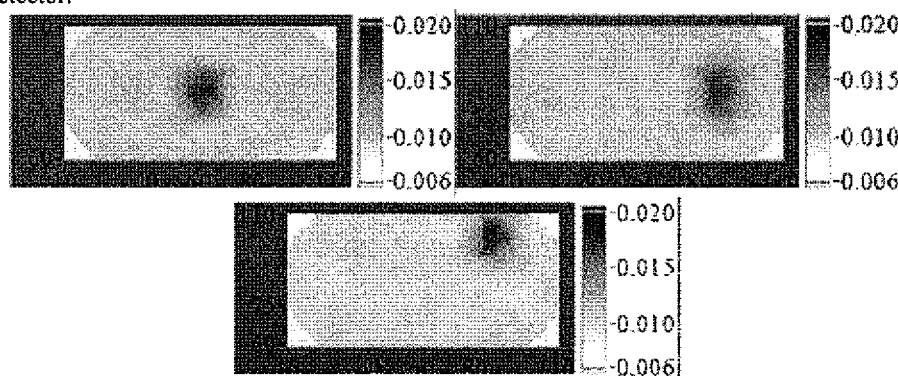


Fig. 6. Reconstructed set of images of the test target at different (a) vertical positions (b) lateral positions along the central line, and (c) lateral positions along

the surface, using the slab reflectance and transmittance geometry of sources and
detectors as shown in Fig. 2 (d).

### 3.1.5 Slab Fan-Beam Imaging

The fan-beam geometry for slab breast imaging is an obvious choice since it can involve the
use of parallel detection through a CCD or other parallel detectors, which are highly stable
and provide robust detection. The simplicity of translating the source across the upper
surface of the tissue is beneficial, but it is not clear how the loss of reflectance information
will affect the reconstructed images of the tissue interior. The geometry used in this section
was as shown in Fig 2.(e), with 5 mm between neighbouring fibers. In these simulations, the
asymmetry is similar to the previous section, so that the same set of simulations were carried
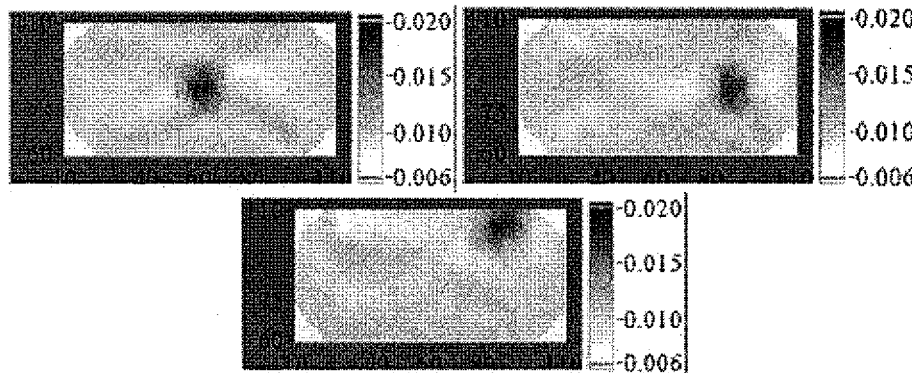out to examine the imaging field sensitivity, shown in Fig. 7.



Fig. 7. Reconstructed set of images of the test target at different (a) vertical
positions (b) lateral positions along the central line, and (c) lateral positions along
the surface similar to those in Fig. 6, using fan-beam slab imaging. Color bar at
right is in absorption coefficient units of mm$^{-1}$.

### 3.1.6 Sub-surface Imaging – Flat boundary

The flat boundary is perhaps one of the most often used geometries for near-infrared sub-
surface imaging because it is simple, readily available clinically in many body locations, and
lends itself to analytic reconstruction methods. This geometry was tested here with 16
sources and 16 detectors all located on the upper surface of the tissue volume producing 256
projections through the medium, spaced alternating at in Fig. 2 (f), with 2.5 mm between
each. The high number of sources and detectors was employed to provide the best
performance that we could obtain in this geometry. The test object was translated vertically
down from the surface, as with the sub-surface imaging on the circular mesh (*Section 3.1.3*),
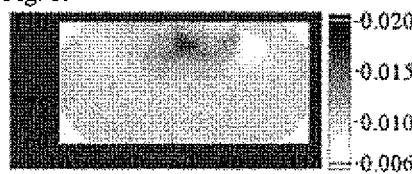with the results shown in Fig. 8.



Fig. 8. Reconstructed set of images where the test target was translated vertically
from the middle of the tissue volume (25 mm down) up to the surface, using 16
sources and 16 detectors alternated and equally spaced along the upper surface of
the region, as illustrated in Fig. 2 (f).

### 3.2 Comparison of Geometries – Contrast and Noise

The above simulations do not completely define the characteristics of the imaging geometry and slight improvements can be achieved for individual cases by adjusting the regularization parameter both during an iteration and spatially-distributed across the imaging plane [15]. Nonetheless comparing the reconstructed peak values in the target zone and the typical noise in the homogeneous background of the image are useful measures of the ability to reconstruct objects accurately. In Fig. 9 (left-top graph) the reconstructed peak values for each target are plotted for changes in vertical position through the image plane. Fig. 9 (right-top graph) is a plot of the standard deviation of the noise within what should be the homogeneous regions of the resulting images. In the peak absorption coefficient, if the value is within 20% of the original target it is considered acceptable. This criterion is simply based upon the typical variations in reconstructed properties observed in previous studies [16].
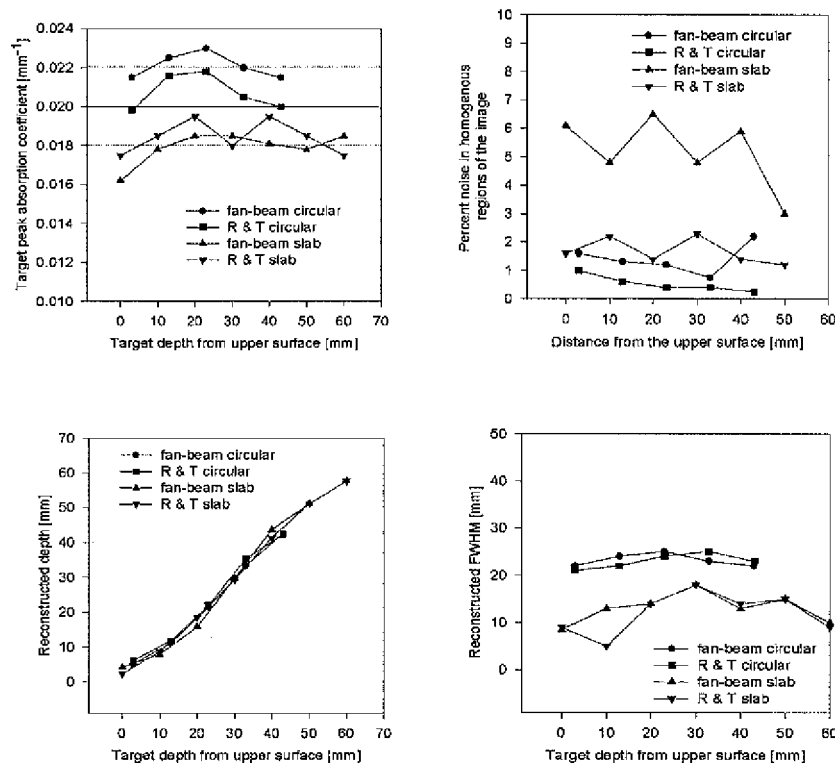


Fig. 9. Calculated (left-top graph) peak absorption coefficient values for the object at different positions within the simulated phantoms, and (right-top graph) reconstructed noise in the background region of the image measured by sampling of random regions of interest outside the target zone. The true value in the first graph is shown with a solid horizontal line, and the 20% region of acceptability is defined by the dotted lines. Calculated (left-bottom graph) target location as a depth from the upper surface, and (right-bottom graph) the calculated target full width at half maximum (FWHM) height as a function of depth in the medium, here taken as an average of the lateral and vertical directions.

A comparison of the three subsurface imaging geometries is shown in Fig. 10, using the same criteria of acceptable peak reconstruction value, as shown in Fig. 9. The reconstructed peak absorption coefficient values for the single targets are shown in Fig. 10 (left-top) as a

function of the depth into the medium, and typical noise values are plotted in Fig. 10 (right-top). In this case, the only geometry which was able to reconstruct accurate absorption coefficient values over a moderate range of depths was with the 8x8 circular arc and the reconstructed peak values decrease significantly with depth for all three sub-surface imaging geometries.
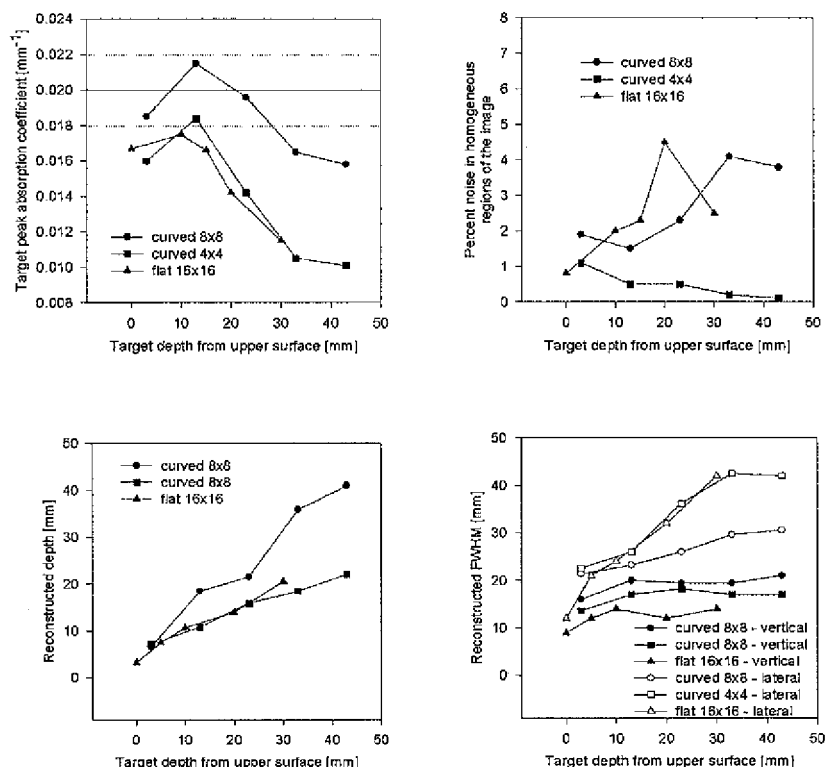


Fig. 10. Calculated (left-top graph) peak absorption coefficient values for the target zone at different positions within the simulated phantoms, and (right-top graph) reconstructed noise in the homogeneous background region of the image outside the target zones. Calculated (left-bottom graph) target location as a depth from the upper surface, and (right-bottom graph) the calculated target full width at half maximum (FWHM) height as a function of depth in the medium, measured here both in the lateral and vertical directions.

### 3.3 Imaging Fields with Multiple Targets

In addition to imaging single objects it is important to recover more complicated distributions, so an additional test has been constructed to compare multiple targets in the circular and slab geometries. The test field contained three targets positioned at different depths, as illustrated in the circular and slab schematic images in the left column of Fig. 11. In this case, two targets were 20 mm in diameter with one in the exact center of the field and one on the right edge at the surface (and upper region in the slab case). The third target had a 10 mm diameter and was located on the left edge of each image (and towards the bottom surface in the slab). All three targets presented a contrast of 2:1 in absorption. The resulting reconstructions for reflectance and transmittance geometries are shown in the middle column while fan-beam reconstructions are contained in the right column of Fig. 11. The image

quality of the two sub-surface geometries is clearly limited in depth resolution, so that the same tests have not been applied to these cases. Therefore, a separate multi-target test consisting of two sub-surface objects, both 10 mm diameter and 2:1 in contrast but with one on the surface and the other 5 mm below, was used to compare these sub-surface configurations, as shown on the left of Fig. 12. The reconstructed images using the 4x4 and 8x8 circular arcs and the 16x16 flat slab are presented in the right columns of the figure.
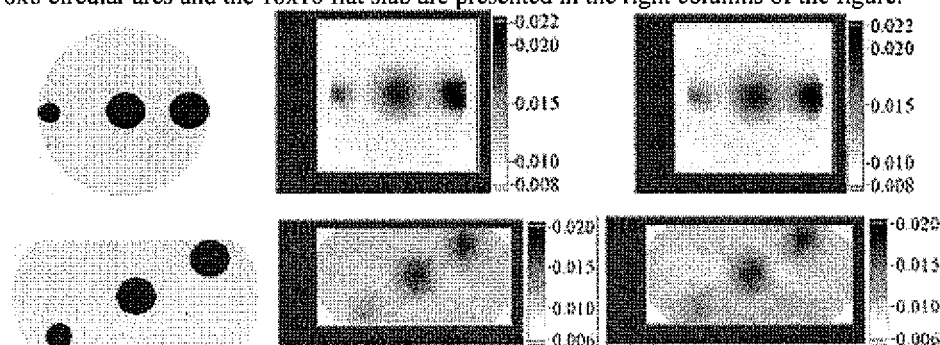


Fig.11. Reconstructed images of three localized targets within a homogeneous background field, (schematics shown in the left column) using geometries of (upper middle) circular reflectance & transmittance (upper right) circular fan-beam, (lower middle) slab reflectance & transmittance, and (lower right) slab fan-beam. The test targets (left) were all 2:1 absroption contrast from the background, and the two on the right were 20 mm diameter, while the one on the left is 10 mm in diameter.
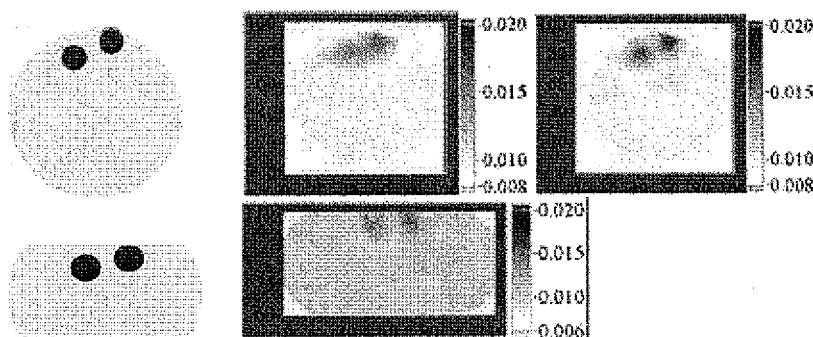


Fig. 12. Reconstructed images of the test fields (shown in the left colum) are displayed at right. The test fields contained two 10 mm diameter objects with one on the surface and the other 5 mm below the surface. In the top row, the middle image shows the result of the 4 source-4 detector array while the right image shows the result from the 8 source-8 detector array. In the bottom row, the result from the slab geometry is shown using the 16 source-16 detector array.

### 3.5 Imaging Fields with Layered Structure

A third test was performed to examine the influence of geometry on the ability to recover a layered structure within the medium. In this situation, the field consisted of three concentric layers of differing absorption coefficient with a single circular inhomogeneity located within the layers. The schematic of the test object is shown in Fig. 13 in the left column, with the circular test field in the upper row, and the corresponding slab test field in the lower row. The reconstructed images using the full reflectance & transmittance and fan-beam approaches are shown in the center and right columns of the figure, respectively. Interestingly, in all cases the circular target could be localized and reconstructed to within

20% of the true value, but the layered structure near the surface was best recovered in the circular geometry. In particular, the full reflectance and transmittance array provided a better reconstruction of the layered structure than did the fan-beam approach, while both slab approaches were dominated by artifacts in the background.

In Fig. 14, the same layered test fields as in Fig. 13 were used to evaluate the sub-surface imaging geometries. These methods were not expected to reconstruct the lower regions of the phantom, but the upper layers and the presence of the object can be partially reconstructed in all cases. The 4x4 detector strategy and the slab 16x16 scheme cannot fully discriminate the object from the layers, while the 8x8 arc geometry can partially reconstruct both the layers and the presence of the object.
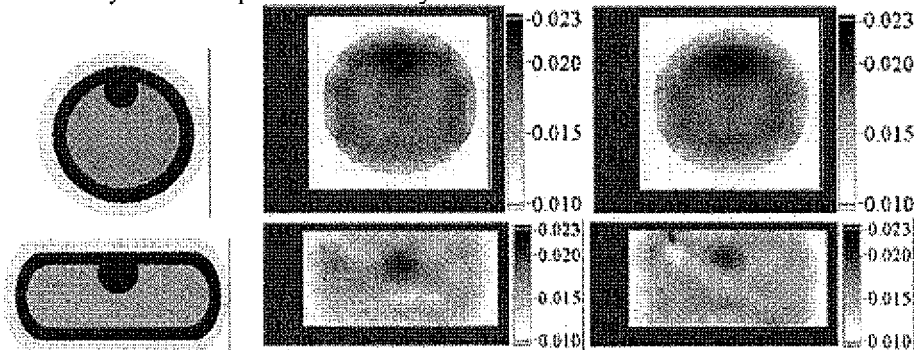


Fig. 13 Tomographic reconstructions of a layered tested field with a single target included for both circular (top row) and slab (bottom row) geometries, with two 5 mm thick layers of $\mu_a = 0.01$ and $\mu_a = 0.02$, with the interior at $\mu_a = 0.015$ mm$^{-1}$, and a 20 mm diameter object at $\mu_a = 0.02$ mm$^{-1}$. The images in the left column represent the test field, while the middle row of images show the full reflectance and transmittance images, and the right column of images show the fan-beam images.
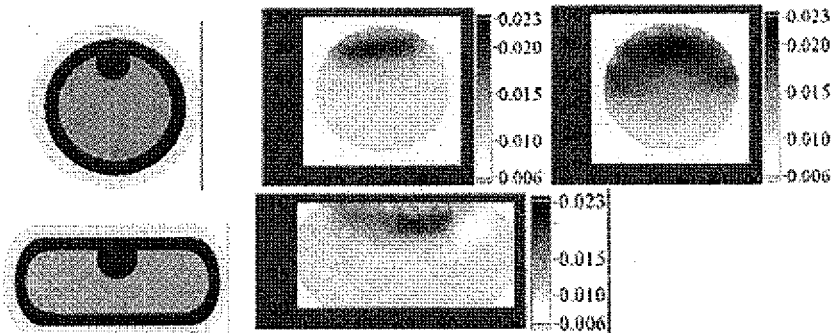


Fig. 14. Reconstructions of the test fields shown on in the left column using the sub-surface imaging geometires, including the curved boundary with (upper middle image) 4 sources and 4 detectors, (upper right image) 8 sources and 8 detectors in an arc, and the slab boundary (lower right image) 16 sources and 16 detectors in a flat plane along the surface.

*3.5 Application to Irregular Tissue Geometries – Cerebral Hemoglobin Imaging*

In an effort to consider these source-detector arrangements in a more realistic geometry, a magnetic resonance image of a human brain was segmented into a finite element mesh (shown in Fig. 15) and used to simulate imaging with the three source-detector geometries (i) fan beam (ii) reflectance and transmittance and (iii) sub-surface imaging. The head size was scaled to that of a neonate, and typical optical properties were applied to the skin, bone, grey

matter and white matter [7,33]. A 15 mm diameter inclusion was added in the upper left of the brain with $\mu_a = 0.03$ mm$^{-1}$, representing a 50% increase from the grey matter, and a 200% increase from the white matter. The initial guess for the image was a homogeneous head shape with $\mu_a = 0.01$ mm$^{-1}$. The inclusion was observed in all reconstructed images with a peak value within 10 % of the true value, indicating that it can be successfully characterized with all three source-detector geometries using this algorithm. Interestingly, none of the imaging geometries could discriminate the white matter structure from the grey matter, but the full reflectance and transmittance method was able to recover the skull optical properties accurately, as was the sub-surface imaging geometry. Also the fan-beam approach produced significant artifact into the image, as a ringing structure. Surprisingly the fan-beam approach recovers the presence of the object clearly, albeit not at a accurate contrast level.
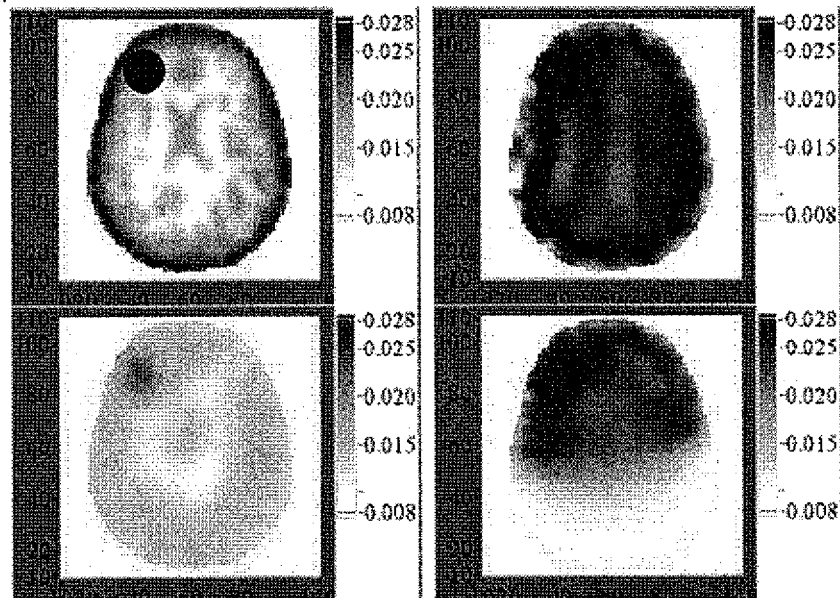


Fig. 15. Reconstructed simulations of a human cranium with the test field (upper left), showing absorption coefficients of skin, $\mu_a = 0.01$, skull, $\mu_a = 0.025$, grey matter, $\mu_a = 0.02$, and white matter, $\mu_a = 0.01$ mm$^{-1}$, with a fixed scattering coefficient of $\mu_s' = 1.0$ mm$^{-1}$. An artificial inclusion having $\mu_a = 0.03$ was included in the upper left of the test field. The reconstructed images are shown using full reflectance and transmittance imaging (upper right), fan beam imaging (lower left), and 8x8 sub-surface imaging with the detectors in an arc around the upper half of the head (lower right). Note that the sub-surface geometry is not expected to recover properties in the lower half of the image.

## 4. Discussion

### 4.1 Geometry Effects in the Reconstructed Image

Determining the optimal source-detector and tissue geometry is not as simple of a task as it might first appear because of the interplay between theoretical performance and practical constraints, so that some theoretically optimal designs must be considered in light of experimental limitations. As a result, all of these issues cannot be fully characterized by the simple simulations contained in this paper. Also, the reconstruction algorithm could be better tailored to any of the specific geometries than in its present generalized form, by altering the regularization scheme to improve the reconstruction to provide a more homogeneous solution across the imaging field [15]. In the cases shown here, the regularization parameter was

chosen to provide optimal reconstructions, through a series of trials, so that the images shown here are our best versions. However, even with these uncertainties about regularization, there are some reconstruction results which are indicative of the measurement data quality which can be used to evaluate and compare the individual geometries. Our goal has been to determine if the geometry significantly inhibits the ability to accurately reconstruct optical properties, or if the geometry adds artifacts to the resulting image which are not easily avoided.

When comparing reconstruction geometries, it would be ideal to have the same number of measurements in the data set, so that changes in geometry are not confounded by changes in the conditioning of the matrix; however, in practice the physical size of the source and detector fibers can limit the number of possiblilities which are available for a given geometry. For example, in the circular geometry, the minimum tissue diameter and the diameter of the fibers dictates the number of sources and detectors that are possible. For these reasons, we have chosen to compare geometries and source-detector arrangements which are physically realistic, while trying to maintain the maximum number of measurements in each data set. The fan-beam and sub-surface imaging schemes can be thought of as sub-sets of the data measured in the full reflectance and transmittance mode, so that it is not surprising that there is some loss of image resolution with each of these two methods. We have also constrained the problem to be 2-dimensional in these cases, however based upon previous experience we anticipate that similar results are obtained in 3-dimensions. Also fully 3-dimensional reconstruction is inherently difficult to interpret, and often requires separation into 2-d slices in order to fully evaluate the image quality. For these reasons, the 2-dimensional images shown here are thought to be representative of the available image quality for each respective geometry.

*4.2 Single Targets*

In the video sequences of Figs. 3 to 8, the object is localized accurately in all cases, and is close to the original true value at most locations (as shown in Fig. 9). Small deviations from the true value can be compensated with changes in the regularization parameters [15], but large deviations from the true value which are accompanied by significant noise in the image cannot generally be eliminated. An example of this phenomenon is observed in Fig. 7, where the fan-beam slab reconstructions show a marked increase in noise within the image, while there is no decrease in the recovered peak height of the target. This noise is likely due to the decreased angles of projection which are used to sample the field, producing regions within the image which cannot be well charaterized by the solution to the inverse problem. Maximizing the number of different angular projections through the field is likely the best way to improve the accuracy of the inverse solution.

Recovering images in the sub-surface imaging geometry is more challenging than with full tomographic methods, and this is expected since the tissue cannot be sampled as effectively ina purely reflectance mode. The most important observation from the data in Fig. 9 is that the true value of the object is not easily recovered without being able to sample measurements in an arc around the tissue sample, as is the case with the 8 source-8 detector array in the circular geometry. By adjusting the regularization parameters, it would be possible to reconstruct the peak values for all three geometries used here, as long as the depth of the target is not lower than 20-30 mm. At depths below 30 mm, the photon paths cannot sample the target effectively. In general as the target is lowered into the medium, the reconstructed peak value will decrease.

*4.3 Multiple Targets*

When multiple targets are present as in Figs. 11 & 12, the circular geometries tend to over-reconstruct targets on the periphery. This problem can be compensated with a radial variation in the regularization parameter [15]. The slab geometries do not recover the smaller test target as well as their corresponding circular geometries. There are no clear

differences between the fan-beam style versus the full sampling of reflectance and transmittance, other than the expected increase in background noise in the fan-beam case. The subsurface imaging method suffers from a field sensitivity which decreases with depth into the tissue, such that lower lying objects are not as strongly reconstructed as objects immediately at the surface.

*4.4 Layered Fields*

When layered test fields are used, there is serious degradation of the image quality in the case of the slab geometry (Fig. 13), whereas both circular geometries were able to provide reasonable images of the subsurface ring and the upper inclusion. Again, the full reflectance and transmittance circular mode provided a slightly more accurate reconstruction of the test field than the fan-beam circular mode. Note that the layer in the circular fan beam reconstruction is closer to the center than in the original test field (Fig. 13). All three sub-surface imaging method are able to reconstruct parts of the layered structure, but only the 8x8 detection method is sufficient to recover the inclusion quantitatively below the layer. It is likely important to ensure that the diffuse projections sample below the suspected inclusion in order to produce an accurate reconstruction of the target. This layered test field is important, since almost all in vivo tissues have a complex layered structure near the surface that may not be clearly resolved unless a circular reflectance and transmittance geometry is used.

*4.5 Cranial Imaging*

For the cranial images in Fig. 15, the complex structure between white and grey matter is not well resolved, which agrees with the observations of other investigators [33]. The location of the skull is well resolved with the full reflectance and transmittance method, but the interior is not. The sub-surface imaging geometry provides a method sufficient to quantify the optical properties of the inclusion. The fan-beam imaging appears to image asymmetric regions, such as the inclusion quite well but cannot recover the skull or brain details at all. In general, the white/grey matter variations which appear on a sub centimeter scale cannot be resolved; however, larger changes in the optical properties, such as the artificial target in the upper left, can be resolved given. It is also likely that absolute changes in the optical properties can be better resolved than the absolute magnitude of the property itself, whereas only the latter case has been tested here. Further study is needed to determine the increase in image quality which is possible with incorporation of MRI-derived initial guesses of the optical property distribution, and other enhancments of the reconstruction process through adaptive spatial regularization or constraints [7, 40].

**5. Conclusion**

In general, increasing the number of measurements improves the quality of the reconstructed images and the image accuracy. Care must be taken to ensure that the projections used provide a homogenous sampling of the entire tissue region of interest, and that the projections maximize the number of angles over which measurments are recorded. The ability to resolve objects improves as the distribution of angular projections increases through the sample; so, the maximum angular coverage of a tissue results from the circular geometry with full sampling of the reflectance and transmittance light, which is demonstrated to have the best image quality in these simulations. The technological simplification of using a fan beam approach is attractive and comes at only a modest decrease in image quality, so this may provide the most practical method for optical imaging. The fan beam approach produces measurmements which are all near the same order of magnitude in intensity so that variable attenuation is not required in the data acqusition system.

A comparison of slab-geometry imaging to circular-geometry imaging with single objects does not demonstrate a major difference in the image quality, but the ability to image layered objects with the slab-geometry was seriously compromised. From these simulations,

we anticipate that the slab geometry is not well suited to imaging layered structures, and this may be due to the relatively few projections at varying angles through the layers which exist. Sub-surface imaging produces the lowest quality images, but is able to quantify absorbing perturbations near the surface. Objects lower than 2 cm are not likely to be imaged accurately by subsurface methods unless the overlying surface is curved. Curved surfaces allow the light projections to probe deeper into the tissue and can provide accurate images of sections of a tissue. The image quality for all geometries presented in this paper is compromised by the generality of the inversion algorithm, so that some improvements can potentially be incorporated for each particular geometry through spatially distributed regularization methods or adaptive regularization [15].

# *In vivo* local determination of tissue optical properties: applications to human brain

Frédéric Bevilacqua, Dominique Piguet, Pierre Marquet, Jeffrey D. Gross, Bruce J. Tromberg, and Christian Depeursinge

Local and superficial near-infrared (NIR) optical-property characterization of turbid biological tissues can be achieved by measurement of spatially resolved diffuse reflectance at small source–detector separations (<1.4 mm). However, in these conditions the inverse problem, i.e., calculation of localized absorption and the reduced scattering coefficients, is necessarily sensitive to the scattering phase function. This effect can be minimized if a new parameter of the phase function $\gamma$, which depends on the first and the second moments of the phase function, is known. If $\gamma$ is unknown, an estimation of this parameter can be obtained by the measurement, but the uncertainty of the absorption coefficient is increased. A spatially resolved reflectance probe employing multiple detector fibers (0.3–1.4 mm from the source) is described. Monte Carlo simulations are used to determine $\gamma$, the reduced scattering and absorption coefficients from reflectance data. Probe performance is assessed by measurements on phantoms, the optical properties of which were measured by other techniques [frequency domain photon migration (FDPM) and spatially resolved transmittance]. Our results show that changes in the absorption coefficient, the reduced scattering coefficient, and $\gamma$ can be measured to within $\pm 0.005$ mm$^{-1}$, $\pm 0.05$ mm$^{-1}$, and $\pm 0.2$, respectively. *In vivo* measurements performed intraoperatively on a human skull and brain are reported for four NIR wavelengths (674, 811, 849, 956 nm) when the spatially resolved probe and FDPM are used. The spatially resolved probe shows optimum measurement sensitivity in the measurement volume immediately beneath the probe (typically 1 mm$^3$ in tissues), whereas FDPM typically samples larger regions of tissues. Optical-property values for human skull, white matter, scar tissue, optic nerve, and tumors are reported that show distinct absorption and scattering differences between structures and a dependence on the phase-function parameter $\gamma$. © 1999 Optical Society of America

*OCIS codes:* 170.7050, 290.4210, 170.3660, 170.5280, 170.4550, 170.6510.

## 1. Introduction

Probing the optical properties of biological tissues has a major effect in several medical applications for diagnosis and therapy. For example, the knowledge of these properties is necessary for optimizing techniques such as near-IR spectroscopy or photodynamic therapy. The scattering and the absorption characteristics of many different kinds of tissues have been reported in the literature.[1] However, they have been most often measured *in vitro*. Because of unavoidable alterations in excised samples, such as blood drainage, structural alterations, and temperature changes, these values are questionable and *in vivo* measurements are preferred.

Measurement of optical properties performed *in vivo* could also be used as a diagnostic tool, which is complementary to other optical biopsy techniques, e.g., tissue autofluorescence. Indeed light scattering and absorption can provide information both on tissue structure and on chromophore content, features that can be used to distinguish between normal tissues, malignant lesions, and other pathologies. For example, hemoglobin and water content have been found to be significantly different in normal and cancerous tissues.[2,3] Differentiation between normal and malignant bladder tissues[4] was found to be possible from the elastic scattering and absorption properties.

F. Bevilacqua, D. Piguet, P. Marquet, and C. Depeursinge (christian.depeursinge@epfl.ch) are with the Department of Micro-Engineering, Institute of Applied Optics, Swiss Federal Institute of Technology Lausanne, 1015 Lausanne, Switzerland. J. D. Gross and B. J. Tromberg are with the Laser Microbeam and Medical Program, Beckman Laser Institute and Medical Clinic, University of California, Irvine, 1002 Health Sciences Road East, Irvine, California 92612. J. D. Gross is also with the Division of Neurological Surgery, University of New Mexico School of Medicine, Albuquerque, New Mexico 87131.

Researchers have proposed different methods to determine quantitatively absorption and reduced scattering coefficients *in vivo*, by using spatially[5-7] and/or temporally resolved measurements.[2,3,8,9] Besides organs such as breast or neonatal brain, which can be transilluminated, measurements of thick tissues can be made in reflectance geometry. The case in which source–detector separations are larger than several transport mean-free paths, corresponding typically to distances greater than 5 mm for biological tissues, has been extensively studied theoretically and experimentally. Diffusion theory or Monte Carlo simulations have been commonly used to relate the measured light intensity to the optical coefficients. In particular, optimized source–detector separations have been calculated by different authors[6,10] to ensure the best sensitivity to absorption and scattering coefficients from spatially resolved reflectance data. For typical turbid tissues, the optimal determination of both absorption and scattering properties requires reflectance measurement at small and large distances. For example, measurements were performed by Farrell *et al.*[5] using distances from 1 to 10 mm and by Bays *et al.*[6] using distances from 3.6 to 15 mm or 2 to 14 mm.

Nevertheless in all these studies the turbid medium is considered homogeneous or made of homogeneous layers. Our approach is different. We wish to characterize optically a small volume of tissue, of the order of a few cubic millimeters, possibly distinct from surrounding tissues. Therefore our goal is to differentiate a small tissue heterogeneity instead of determining average optical properties of a large volume of tissue. To achieve this, we chose to perform spatially resolved reflectance measurements with only small source–detector separations, from 0.3 to 1.4 mm, even if these distances are not optimal for absorption determination.

Mourant *et al.*[4,11] have shown that the absorption coefficient can be estimated from measurement at a single distance of ~1.7 mm, assuming the scattering coefficient to be in a certain range. They have also shown that measurements at a single shorter distance (~0.2–0.3 mm) allows monitoring of spectroscopic variations in the scattering properties of tissues. In this research we address a general case in which both tissue scattering and absorption properties are simultaneously estimated from measurements at distances smaller than 1.4 mm.

The theoretical framework for interpretation of the measured profile in terms of absorption and scattering properties[12,13] was given in a previous study based on Monte Carlo simulations. The role of the phase function at short source–detector separations was carefully studied. In particular, we showed that, besides absorption and reduced scattering coefficients, a parameter depending on the first and the second moment of the phase function must be taken into account for source–detector separation ranging approximately from 0.3 to 10 transport mean free paths. This analysis is more complete compared with previous research in which only the first mo-

ment of the phase function (the anisotropy factor) was considered.

First we describe the probe design and the Monte Carlo model developed to simulate the measured profile. Second we discuss the average tissue volume probed and sensitivity to medium boundaries from experiments and simulations. Third we describe how the scattering and the absorption properties of tissues can be deduced from reflectance data. The accuracy of the proposed procedure is demonstrated on phantoms, the optical properties of which are measured by others techniques. Finally we present and discuss measurements of human brain obtained *in vivo*. These clinical measurements were performed in parallel with a complementary method, frequency domain photon migration (FDPM),[2,3] which probes a larger tissue volume. Optical properties from FDPM measurements are compared with values that we obtained by the spatially resolved method described here, using small source–detector separations.

## 2. Materials and Methods

### A. Definitions

The spatially resolved reflectance is denoted $R(\rho)$, where $\rho$ is the source–detector separation. It is defined by the backscattered power received by a detector per unit area for a source of power unity. In our measurements $\rho$ ranges between 0.3 and 1.4 mm.

The optical properties of tissues are the average refractive index $n$ of the medium, the absorption coefficient $\mu_a$, the scattering coefficient $\mu_s$, and the phase function $p(\cos\theta)$, where $\theta$ is the scattering angle. The phase function is the probability density function for $\cos\theta$. We consider the refractive index of tissues[14] as a constant, $n = 1.4$.

It is also useful to define the reduced scattering coefficient $\mu_s' = \mu_s(1 - g)$ and the transport mean free path, $mfp' = (\mu_s' + \mu_a)^{-1}$, where $g$ is the anisotropy factor and is defined as the average of $\cos\theta$. Generally the reduced scattering coefficient $\mu_s'$ and the absorption coefficient $\mu_a$ are used to characterize optically thick tissue. Indeed for a high albedo medium the light fluence rate depends only on $\mu_s'$ and $\mu_a$ at distances of several transport mean free paths (typically $\rho > 5$ mm for tissues) from the source (diffusion approximation). Therefore use of $\mu_s'$ and $\mu_a$ is a natural choice if measurements are performed at such distances. Because we want to take measurements at closer distances, in the range of one transport mean free path we expect that some parameters of the phase function must be taken into account. This theoretical problem was fully studied with Monte Carlo simulations and reported in Refs. 12 and 13. We consider below only the main implications of this research.

For distances between 0.3 and 10 transport mean free paths we found that the reflectance curve depends on $\mu_a$, $\mu_s'$, and a third parameter $\gamma = (1 - g_2)/(1 - g_1)$, where $g_1$ and $g_2$ are, respectively, the

first and the second moments of the phase function. The $n^{\text{th}}$ moment $g_n$ is defined as:[15,16]

$$g_n = \int_{-1}^{1} P_n(\cos\theta)p(\cos\theta)d(\cos\theta), \qquad (1)$$

where $P_n$ is the Legendre polynomial of order $n$. Note that the first moment $g_1$ is the anisotropy factor $g$. The parameter $\gamma$ is derived from the second-order similarity relations derived by Wyman et al.,[15] which are valid for a second-order anisotropic radiance (i.e., the radiance can be expanded as a series of Legendre polynomials of the order of at most 2). For comparison, note that the diffusion approximation and first-order similarity relation correspond to a first-order anisotropic radiance (i.e., the radiance can be expanded as a series of Legendre polynomials of the order of at most 1). The role of the parameter, $\gamma = (1 - g_2)/(1 - g_1)$, implies that the anisotropy factor $g$ ($=g_1$) alone is not sufficient to predict correctly the reflectance curve close to the source.

From this analysis, each tissue can be potentially characterized by three parameters: $\mu_a$, $\mu_s{}'$, and $\gamma$. However, owing to the restricted range of the source–detector distances that we want to use, the simultaneous determination of $\mu_a$, $\mu_s{}'$, and $\gamma$ is not always possible with a high degree of accuracy. The achievable accuracy depends on the optical properties themselves and on experimental uncertainties. This problem is addressed in Section 3 for both phantom and tissue measurements.

The parameter $\gamma$ may give interesting information about the tissue structure. Indeed, as measured by several authors,[17–20] the tissue phase function can be approximated by summing a highly anisotropic phase function, $p_{HA}(\cos\theta)$, due to large particles, plus a low anisotropic phase function, $p_{LA}(\cos\theta)$, due to small particles:

$$p_{\text{tissue}}(\cos\theta) = (1 - \alpha)p_{HA}(\cos\theta) + \alpha p_{LA}(\cos\theta). \quad (2)$$

The coefficient $\alpha$ is introduced to guarantee the normalization of $p_{\text{tissue}}(\cos\theta)$.

The first term $p_{HA}(\cos\theta)$ has been fitted to the Rayleigh–Gans phase function[21] or to the Henyey–Greenstein phase function,[17,18] $p_{HG}(\cos\theta)$:

$$p_{HG}(\cos\theta) = \frac{1 - g_{HG}{}^2}{2(1 + g_{HG}{}^2 - 2g_{HG}\cos\theta)^{3/2}}. \quad (3)$$

The moments of the Henyey–Greenstein phase function are given by $g_n = g_{HG}{}^n$ ($n > 0$).

The second term, $p_{LA}(\cos\theta)$, can be interpreted as a Rayleigh-scattering contribution, valid for small scatterers compared with the wavelength. It has been approached by a purely isotropic term[17,21] or a Henyey–Greenstein phase function with a low negative $g$ value.[18] We propose using the Rayleigh phase function[16]:

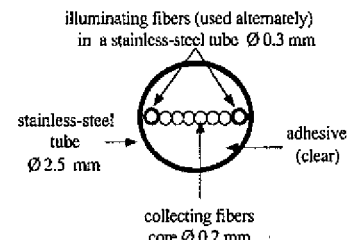$$p_{\text{Rayleigh}}(\cos\theta) = \frac{3}{8}(1 + \cos^2\theta). \quad (4)$$



Fig. 1. Probe for measuring spatially resolved reflectance.

The moments of the Rayleigh phase function are $g_1 = 0$, $g_2 = 0.1$, $g_3 = 0, \ldots$.

Rayleigh scattering contributes nothing to the first moment $g_1$ but only to the second moment $g_2$. The moments of the tissue phase function $p_{\text{tissue}}(\cos\theta)$ given by Eq. (2) are therefore

$$g_1 = (1 - \alpha)g_{HG}, \qquad g_2 = (1 - \alpha)g_{HG}{}^2 + 0.1\alpha. \quad (5)$$

Therefore we see that parameter $\gamma$ is influenced by the relative concentration of Rayleigh scatterer $\alpha$, which should depend on tissue structure.

Published phase-function data suggest possible values of $\gamma$ for biological tissues.[17–20] These phase functions have been measured in goniometric experiments on thin samples. Many artifacts can affect these measurements, such as tissue preparation and tissue thickness, and these results should be used with caution. The phase function reported by Jacques et al.[17] for human dermis at 633 nm leads to $\gamma = 1.4$. The phase functions of white and gray matter at $\lambda = 750$ nm measured by van der Zee et al.[19] give values of ~1.5. Therefore we performed $p_{\text{MHG}}$ simulations with $\gamma = 1.5$ as a starting point. As will be discussed, fitting our experimental data to simulations performed with different values of $\gamma$ estimation permits a reasonable parameter estimation.

## B. Experimental Setup

The probe used for measuring the spatially resolved reflectance is described in Fig. 1. It is a linear array of optical fibers (core diameter, 200 μm; N.A. = 0.37 in air). Two source fibers can be used to illuminate the tissue. They are disposed symmetrically with regard to the collecting fibers. If the sample is homogeneous, the reflectance curve is identical with either illuminating fiber. Therefore comparing the two curves tests the heterogeneity of the investigated tissue region or detects obstructions beneath the illuminating fibers. If the two curves are close (typically with differences of less than 10%), the measurement is validated and the average of the two curves is calculated.

The illuminating fibers are slid into small stainless-steel tubes to avoid direct light coupling with the collecting fibers. The coupling between each collecting fiber has been experimentally measured and found to be less than 2%. The fiber array is set in a stainless-steel tube 2.5 mm in diameter and 20 cm long. The tube is filled with an optically clear adhesive (black adhesive may also be used). The
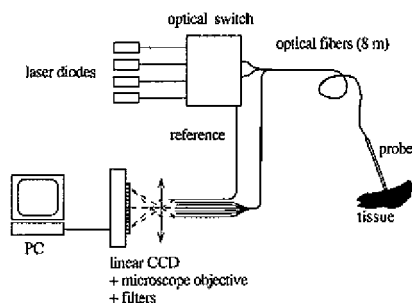
Fig. 2. Experimental setup.



Fig. 3. Comparison between the exact and the simplified boundary conditions. The optical coefficients are $\mu_s' = 1$ mm$^{-1}$, $\mu_a = 0.01$ mm$^{-1}$, and $\gamma = 1.9$.

probe is rigid, which allows for easier handling by the physician, during surgery, for example. The whole probe can be sterilized. The experimental setup is shown in Fig. 2. An optical switch (Dicon Model GP700) is used to select the illuminating fiber from different sources. For the brain measurements, four laser diodes emitting at 674, 811, 849, and 956 nm were used (SDL, Inc. Models 7421, 5420, 5421, and 6321, respectively). Two other laser diodes were used for phantom measurements, emitting at 675 and 828 nm (ILEE LDA 2011 and 1805, respectively). The six fibers that collect the backscattered light are imaged on a linear CCD (Hamamatsu S3921). The signal is digitized by a 12-bit analog-to-digital card. Only one measurement, which takes ~0.1 s, is then needed to measure simultaneously the intensity collected by the six fibers. The entire system is controlled by a personal computer.

Transmission differences between each fiber are corrected by using a measurement on a turbid phantom illuminated uniformly. Immediately after each reflectance measurement, the background light is automatically measured and then subtracted from the reflectance signal. To minimize the background light, a long-pass filter ($\lambda > 650$ nm) is placed between the end of the bundle and the CCD. Even during open surgery where ambient light is substantial, the measured background ranged between 1% and 10% at the farthest fibers, depending on the wavelength used.

### C. Monte Carlo Simulations

A model of photon migration in tissues is necessary to define the relationship between the measured reflectance and the optical properties. Analytical solutions from the diffusion equation are not appropriate in our case because we are interested in the reflectance close to the source, at a distance comparable with the transport mean free path (mfp').[5,7] We performed Monte Carlo simulations to predict the measured reflectance of an homogeneous semi-infinite turbid media. The code that we used was extensively tested.[12,22,23] Any phase function can be implemented in discretized form.

Our simulations take into account the exact diameter of the illuminating and the collecting fibers as well as their numerical apertures (N.A. = 0.26 in tissue). However, the distortion of the signal due to
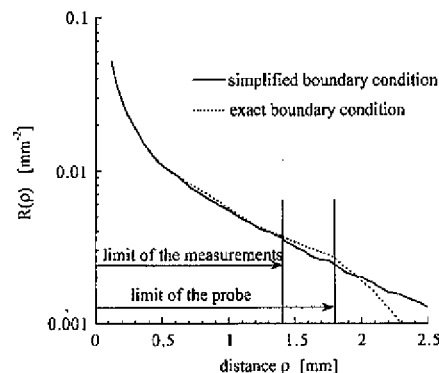
the size of the fibers that we used ($\emptyset = 200$ nm) has an almost negligible influence on the reflectance curve.

The mismatch of the index of refraction at the surface of the medium is also taken into account in our simulation by using the Fresnel law for each photon reaching the surface. Some simulations have been performed with the exact geometry of the probe as described in Fig. 1, taking into account the mismatch of the index of refraction between the probe adhesive ($n = 1.5$) and the sample as well as the mismatch of the index of refraction between the air and the sample outside the probe ($\rho > 1.8$ mm). Photons refracted inside the lumen of the stainless-steel tube are considered absorbed. In Fig. 3 the reflectance obtained with the exact probe configuration is compared with the simplified case of the semi-infinite space ($n_{medium} = 1.4$, $n_{probe} = 1.5$). The exact-probe-boundary condition is extrapolated beyond the surface of the probe to where the boundary is tissue/air. As expected, there are important differences between the exact and the simplified cases for $\rho > 1.5$ mm, close to the limit of the probe. The decreased reflectance at $\rho > 1.8$ for the exact case is due to the increase in internal reflection at the interface between the medium and the air. However, the differences between the exact and the simplified cases are less than a few percent for $\rho < 1.4$ mm, corresponding to the region where the measurements are performed.

The simplified case, assuming cylindrical symmetry, is computationally much less time-consuming than the exact configuration. Exact-configuration simulations require ~10 times the number of photons for statistical errors to be achieved comparable for the simplified case. Indeed in the simplified case the cylindrical symmetry allows for the use of annular detectors to compute the reflectance. The advantage of annular detectors is their larger area, compared with the detector area used in the configuration of the exact-boundary condition configuration. Following the result illustrated in Fig. 3, we decided to employ only the simplified semi-infinite condition and be restricted to $\rho < 1.4$ mm.
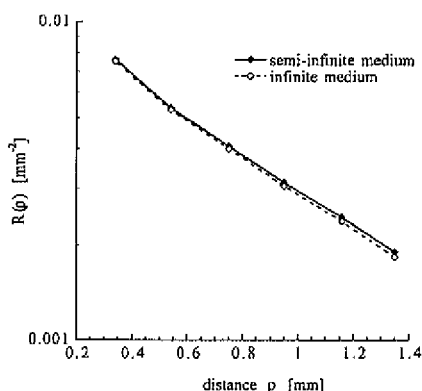
Fig. 4. Comparison between measurements in semi-infinite and in infinite media. The medium is Intralipid. The optical coefficients were measured by the FDPM technique: $\mu_s' = 1.2$ mm$^{-1}$, $\mu_a = 0.0005$ mm$^{-1}$ ($\lambda = 675$ nm).

## 3. Results and Discussion

### A. Boundary Effects

During *in vivo* investigations the ideal case of a medium with a perfect plane surface is never realized. Moreover the probe could be slightly pushed inside the tissue. Therefore the effect of the medium boundary on the measured reflectance is important to quantify experimentally. In Fig. 4 we show two measurements in Intralipid ($\lambda = 675$ nm), one at the surface and the second inside the medium. The difference between these two measurements is less than 5%, which could seem very surprising at first glance. However, as shown by simulation in Fig. 3, the boundary condition outside the probe has only a weak effect on the intensity measured by the six fibers. The boundary condition created by the probe itself, i.e., the index of refraction mismatch between the medium and the adhesive inside the probe, is much more critical.

The negligible effect of the tissue boundaries shown in this section is an important advantage for clinical investigation. This experiment also clearly demonstrates that the sample volume investigated is principally confined to the region just beneath the probe surface. This point is developed further in Subsection 3.B.

### B. Depth of Tissue Investigated

To quantify more precisely the volume of tissue probed in our technique, we determined the depth below the surface of each scattering event in the simulation. With this information we determined the average depth of all the scattering events for each detected photon, which we present as a probability density function in Fig. 5. To permit more general statements, distances are expressed here in mfp' units. For typical turbid tissue[1] and near-IR wavelengths, $\mu_s'$ is around 1 mm$^{-1}$ and $\mu_a$ is less than 0.2 mm$^{-1}$, which means that 1 mfp' $\approx$ 1 mm. Figure 5 shows that the average depth of scattering is around 0.8 mfp'. Moreover it shows that for typical tissue
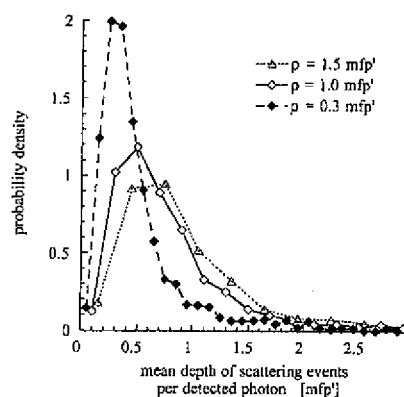


Fig. 5. Probability density of the mean depth of scattering events per detected photon for the case of $\gamma = 1.9$.

optical properties, structures located beneath the probe at a depth greater than 2 mfp' are not likely to contribute significantly to the measured signal (for $\rho < 1.5$ mfp'). These results are consistent with the average depth computed by Weiss *et al.*[24] using Monte Carlo simulations. However, note that their simulations do not take into account any refractive-index mismatch or a restricted numerical aperture of the detector.

To evaluate the maximum depth of photons paths, we performed experiments in Intralipid, placing the probe at the liquid surface and moving an absorbing plate placed horizontally, as described in Fig. 6. The reflectance $R(\rho, d)$ was measured for varying thickness $d$. The ratio $R(\rho, d)/R(\rho, d = \infty)$ is reported in Fig. 6. Figure 6 shows that the intensity of the reflectance is decreased by ~20% if the medium is 2 mfp' thick and by ~10% if it is 3 mfp' thick (for the albedo and the range of $\rho$ considered). These results imply that 80% or 90% of the photons do not penetrate deeper than 2 or 3 mfp', respectively, into the medium. This experiment complements our simulation result (Fig. 5) where the average depth of scat-
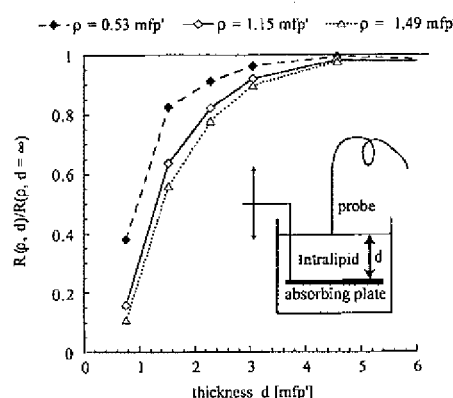


Fig. 6. Effect of the Intralipid thickness on the reflectance. The setup for the investigation of Intralipid with varying thickness is illustrated on the right-hand side. The optical coefficients of Intralipid were measured by the FDPM technique ($\lambda = 956$ nm). The reduced albedo is $a' = \mu_s'/(\mu_s' + \mu_a) = 0.98$.
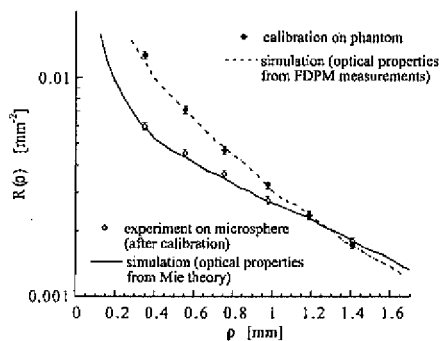
Fig. 7. Calibration measurement of a siloxane phantom and measurement test of a microsphere suspension. The siloxane phantom optical properties were measured with FDPM: $\mu_a = 0.00024 \pm 0.00002$ mm$^{-1}$, $\mu_s' = 1.82 \pm 0.01$ mm$^{-1}$ ($\lambda = 674$ nm). The siloxane phantom measurement is multiplied by the calibration factor to fit the corresponding simulation ($\gamma = 1.8$). The measurement on microsphere suspension is multiplied by the calibration factor derived from the siloxane phantom measurement. The simulation, corresponding to the microsphere suspension measurement, is performed by using the optical properties derived from Mie theory: $\mu_s' = 1.0$ mm$^{-1}$, $\mu_a = 0.0005$ mm$^{-1}$, Mie phase function ($g_1 = 0.916$, $\gamma = 2.2$).



Fig. 8. Relationship between parameters $R(\rho = 1$ mm$)$ and $|\partial_\rho \ln R(\rho = 1$ mm$)|$ and the optical coefficients $\mu_s'$ and $\mu_a$ for cases of $\gamma = 1.5$ and 1.9.

tering was estimated to be ~1 mfp′. Thus for typical biological tissues our measurements are mainly sensitive to the region of tissue located within 2 mm of the surface and the investigated volume is of the order of 1 mm$^3$.

## C. Calibration and Test on Microsphere Suspension

To perform absolute intensity measurements, calibration is performed on a solid turbid siloxane phantom of known $\mu_a$ and $\mu_s'$ (determined independently by FDPM).[2,3] Value $\gamma = 1.8 \pm 0.1$ was determined for the calibration phantom by consideration of the value that gives the best fit to the experimental curve, $\mu_a$ and $\mu_s'$ being fixed ($\lambda = 674$–956 nm).

As shown in Fig. 7 the phantom measurement, scaled by a single factor applied equally to all fibers, fits well the Monte Carlo simulation performed with phantom coefficients. This factor is defined as the calibration factor for a given wavelength. The calibration was performed at the end of each set of clinical measurements.

Experiments on microsphere suspensions (polystyrene sphere $\varnothing$ 1.072 $\pm$ 0.019 $\mu$m) were performed to assess the accuracy of our theoretical model and the calibration method. The scattering coefficient and the phase function of such turbid media can be known precisely by using Mie theory.[25] Because no dye was added to the suspension, $\mu_a$ was considered to be equal to the water absorption. In Fig. 7 measurement of the reflectance is compared with a simulation computed with the microsphere suspension coefficients ($\mu_s' = 1.0$ mm$^{-1}$, $\mu_a = 0.00041$ mm$^{-1}$, $\gamma = 2.2$). The excellent agreement found here between experiments and simulation confirms the accuracy of our simulations and the validity of our calibration procedure.
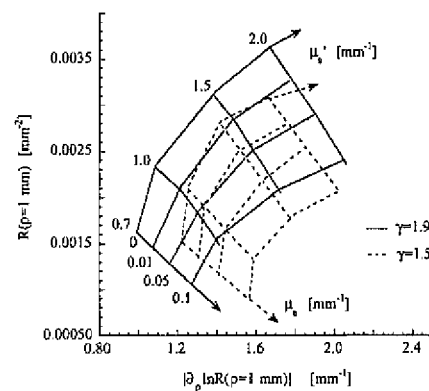
## D. Inverse Problem

Our goal is to solve the inverse problem that consists of extracting optical coefficients from the reflectance data. Measurements of the reflectance intensity $R(\rho)$ and the slope of ln $R(\rho)$ [denoted $\partial_\rho \ln R(\rho)$], determined at a distance $\rho = 1$ mm, can be used to derive $\mu_s'$ and $\mu_a$ for a given $\gamma$ value. Figure 8 shows graphically the relationship between $\mu_s'$, and $\mu_a$ and the two parameters, $R(\rho = 1$ mm$)$ and $|\partial_\rho \ln R(\rho = 1$ mm$)|$. To illustrate the influence of parameter $\gamma$, two examples are superimposed: $\gamma = 1.5$ and $\gamma = 1.9$. We see clearly in Fig. 8 that $\mu_s'$, and $\mu_a$ cannot be determined uniquely from the two parameters, $R(\rho = 1$ mm$)$ and $|\partial_\rho \ln R(\rho = 1$ mm$)|$, if $\gamma$ is unknown. This indetermination may be resolved by the values of $R(\rho)$ and/or $|\partial_\rho \ln R(\rho)|$ at other distances. Therefore the following procedure was defined for tissue measurements:

(1) Determination of $\mu_s'$ and $\mu_a$ from $R(\rho = 1$ mm$)$ and $|\partial_\rho \ln R(\rho = 1$ mm$)|$ for discrete values of $\gamma$ (for example, $\gamma = 1.0, 1.5, 1.9, 2.2$).
(2) Simulations with different sets of $\mu_s'$ and $\mu_a$ obtained from Eq. (1).
(3) Comparison between the simulations and the reflectance profile for distances $0.35 < \rho < 1.4$ mm.

This last step permits us to determine the value of $\gamma$ that gives the best fit. Points (1)–(3) can be done iteratively to evaluate $\gamma$ more precisely. The precision that can be obtained depends on the optical coefficients themselves and on the experimental uncertainties. Nevertheless two important technical points should be noted:

First, determination of $\mu_s'$ is only weakly influenced by $\gamma$ for $\mu_s'$ close to 1 mm$^{-1}$. Indeed in Fig. 8 the differences induced by $\gamma = 1.5$ or $\gamma = 1.9$ are typically 10% for $\mu_s'$. In contrast, the absolute determination of $\mu_a$ is critically sensitive to $\gamma$. However, if $\gamma$ remains constant, relative variations of $\mu_a$ can still be precisely evaluated. This point is discussed with the results obtained from Intralipid measurements in Subsection 3.E. Metabolism moni-

toring or drug monitoring could therefore be a potential application of such a probe.

Second, the experimental determination of $|\partial_\rho \ln R(\rho = 1 \text{ mm})|$ requires measurements at different distances close to 1 mm. To minimize errors on $|\partial_\rho \ln R(\rho = 1 \text{ mm})|$ due to experimental artifacts, we performed a fit of the reflectance curve (0.5 mm $< \rho$ 1.4 mm) with the function $m_1\rho^{m_2}\exp(-m_3\rho)$, which was always found to fit Monte Carlo simulations well for this restricted range of distances. (The same function was also proposed by Bolt and ten Bosch.[26]) Parameters $R(\rho = 1 \text{ mm})$ and $|\partial_\rho \ln R(\rho = 1 \text{ mm})|$ are then derived from the fit. Once optical coefficients $\mu_a$ and $\mu_s'$ are derived, the validity of this procedure is double-checked by comparing the curve obtained from the Monte Carlo simulation with the experimental profile.

### E. Phantom Measurements

We present in this subsection measurements on tissuelike phantoms (Intralipid and microsphere suspensions). Measurements of phantoms with varying $\mu_a$ and $\mu_s'$ values were used to test the inversion procedure. For the Intralipid measurements we considered the $\gamma$ value as *a priori* not known, even though $\gamma$ can be estimated from published research (described below). The phantoms made of Intralipid and dye [iron(III) ferrocyanide] at different concentrations were calibrated by the FDPM technique (performed at large source–detector separations and therefore insensitive to $\gamma$). For Intralipid measurements, reflectance profiles were found to fit best when the parameter $\gamma$ was between 1.6 and 1.8 for $\lambda = 674$–849 nm. The $\mu_a$ values derived from our method are plotted in Fig. 9(a) versus the values obtained by the FDPM technique. Figure 9(a) shows that $\gamma = 1.8$ leads to an overestimation of $\mu_a$ by ~0.005 mm$^{-1}$, whereas $\gamma = 1.6$ leads to an underestimation of $\mu_a$ by ~0.01 mm$^{-1}$. This example clearly illustrates that determination of the absolute values of $\mu_a$ are sensitive to $\gamma$. However, changes in the absorption coefficient can be measured to within $\pm 0.005$ mm$^{-1}$.

The accuracy of the inversion procedure on $\mu_s'$ is illustrated in Fig. 9(b). In the case of $\mu_s'$, as mentioned above, the influence of $\gamma$ is weaker than in the case of $\mu_a$. A difference of only 5% is found on the $\mu_s'$ if $\gamma = 1.6$ is used instead of 1.8. This is also approximately the variation in $\mu_s'$ values obtained by multiple FDPM measurements. We also found that in the case of a constant Intralipid concentration the measured values of $\mu_s'$ vary by less than 2% when $\mu_a$ is increased from 0.012 to 0.5 mm$^{-1}$ by the addition of dye, which proves that the data-inversion procedure effectively uncouples $\mu_a$ and $\mu_s'$.

From our measurements, $\gamma$ can be estimated to $\gamma = 1.7 \pm 0.1$ ($\lambda = 675$ nm). The calculation when Mie theory was used and the size distribution given by van Staveren *et al.*[27] leads to $\gamma = 1.89$ ($\lambda = 675$ nm). These values are in good agreement considering that the actual size distribution of the sample may slightly vary from the sample measured by van Staveren *et*
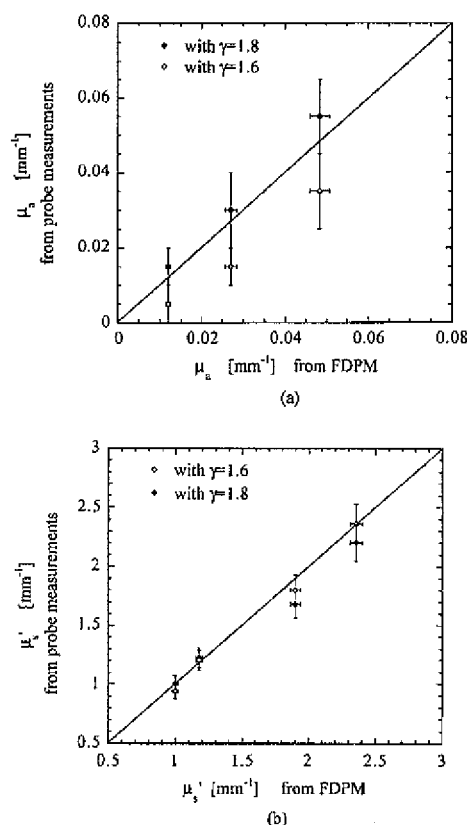


Fig. 9. Comparison between (a) $\mu_a$, and (b) $\mu_s'$ obtained by the FDPM technique and by probe measurements. Measurements are on Intralipid [(a) with dye; (b) without dye].

*al.* Note also that they found a similar discrepancy for $g_1$ between Mie theory and experiments.

Further assessments of the inversion procedure were performed on monodisperse microsphere suspensions. In this case we considered the $\gamma$ value as *a priori* known from Mie theory: $\gamma = 2.2$ (polystyrene, $\phi = 1.053 \pm 0.010$ μm, $\lambda = 675$ nm). The optical coefficients derived from our local reflectance measurements are compared with values obtained with a spatially resolved transmittance method described elsewhere.[22,23]

Figures 10(a) and 10(b) show $\mu_a$ and $\mu_s'$ values obtained by both methods: spatially resolved transmittance and reflectance. Phantoms made of microsphere suspensions and ink at different concentrations were used. An excellent correlation is found between the $\mu_a$ and $\mu_s'$ values obtained by the two methods. Small systematic differences (typically 10%) are found when comparing absolute values. They are mainly due to errors occurring in the calibration procedures (for both methods). A further comparison with Mie theory also showed a typical deviation of 2% for $\mu_s'$ (a maximum deviation of 10%). The relatively small errors that we found here are typical of errors found when different techniques for measuring turbid-media optical properties are compared.[28] Such errors could be avoided by multiple calibrations on several turbid samples of different
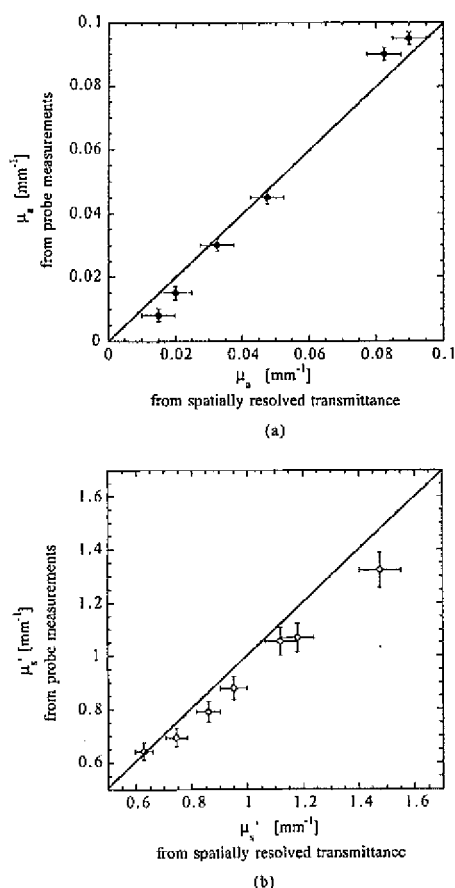
Fig. 10. Comparison between (a) $\mu_a$, and (b) $\mu_s'$, obtained from spatially resolved transmittance (the method described in Refs. 22 and 23) and from probe measurements. Measurements are on microsphere suspensions [(a) with ink; (b) without ink].

known optical properties. However, the accuracy of tissue measurements is subject to other major limitations due to, for example, their structure and heterogeneity.[29] Therefore more accurate calibration is not necessarily required for absolute tissue measurements, since we are mainly interested in observing optical-property differences between tissue physiological states.

### F. *In vivo* Measurements on Brain Tissues

Clinical measurements of normal and malignant neural tissues were recorded *in vivo* during brain surgery.[30] Two different cases are reported here. Case 1 was a 3-year-old male and case 2 was an 8-year-old male. Different types of tissues were investigated in each case. Several measurements (typically six) were always performed successively at a given location. The intensity fluctuations (typically of the order of 10%) for these measurements were mainly due to tissue heterogeneity and slight probe movements. The average reflectance was calculated for each location as well as the standard deviation. Note that the uncertainty due to the apparatus, estimated from measurements on a phantom, is much

lower (<5%). Before each set of measurements the blood from the surgical site was carefully irrigated away with saline and the probe was cleaned with a saline-damped sponge. The measurements presented here were performed in parallel with frequency-domain measurements[2,3] (FDPM) by using a source–detector separation of 10–14 mm.

In case 1 measurements were performed on normal cerebral cortex (frontal lobe and temporal lobe), optic nerve astrocytoma (size, ≈1.3 cm), and normal optic nerve. In case 2 measurements were performed on the skull, deep cerebellar white matter with scar tissue (from a previous surgery), medulloblastoma (size, ≈3.8 cm), and deep cerebellar white matter. Tumor dimensions were estimated from conventional imaging techniques (i.e., computed tomography and/or magnetic resonance imaging).

As discussed in Subsection 3.B, the depth probed is less than ~2 mm. For each type of tissue that we investigated the influence of surrounding tissues on the measurement is weak. In particular, only gray matter is investigated during measurements of the cerebral cortical surface.

Figures 11(a) and 11(b) show the measured parameters $R(\rho = 1 \text{ mm})$ as a function of $|\partial \ln R(\rho = 1 \text{ mm})|$ obtained for cases 1 and 2, respectively. They are similar to Fig. 8 except that the relationship between parameters $R(\rho = 1 \text{ mm})$ and $|\partial_\rho \ln R(\rho = 1 \text{ mm})|$ and optical coefficients $\mu_a$ and $\mu_s'$ is indicated only qualitatively by two arrows for better clarity. (Different grids corresponding to different $\gamma$ values should be superimposed.) Quantitative results are reported in Tables 1 and 2.

Figures 11(a) and 11(b) show that parameters $R(\rho = 1 \text{ mm})$ and $|\partial_\rho \ln R(\rho = 1 \text{ mm})|$ provide excellent discrimination between tissue types. The spectroscopic signature on $R(\rho = 1 \text{ mm})$ and $|\partial_\rho \ln R(\rho = 1 \text{ mm})|$ should also be noted. The cortex and the skull exhibit less significant spectroscopic differences compared with tumor tissues such as the astrocytoma and the medulloblastoma. Thus parameters $R(\rho = 1 \text{ mm})$ and $|\partial_\rho \ln R(\rho = 1 \text{ mm})|$ could be useful for optical biopsy. Nevertheless we believe that to exploit these results fully the differences found must be explained in terms of scattering and absorption parameters. These factors in turn can be used to understand physiological and structural variations. The procedure described in Subsection 3.D was used to determine coefficients $\mu_s'$, $\mu_a$, and $\gamma$ from the measured curves. This procedure is fully illustrated for measurements of the temporal lobe. Results of optical coefficient calculations are summarized for all tissues in Tables 1 and 2. Values obtained in parallel by the FDPM technique are also indicated.

Figure 12 shows that the best fit to the cortex (temporal lobe) data is obtained with $\gamma = 1.9$. Lower values, such as $\gamma = 1.5$, led to impossible values for $R(\rho = 1 \text{ mm})$ and $|\partial_\rho \ln R(\rho = 1 \text{ mm})|$ and should therefore be rejected. Larger values, such as $\gamma = 2.2$, do not fit the reflectance data for distances $\rho < 0.8$ mm. The $\gamma$ value is then estimated to be $\gamma = 1.9 \pm 0.2$. Note that $\gamma = 2.2$ would lead
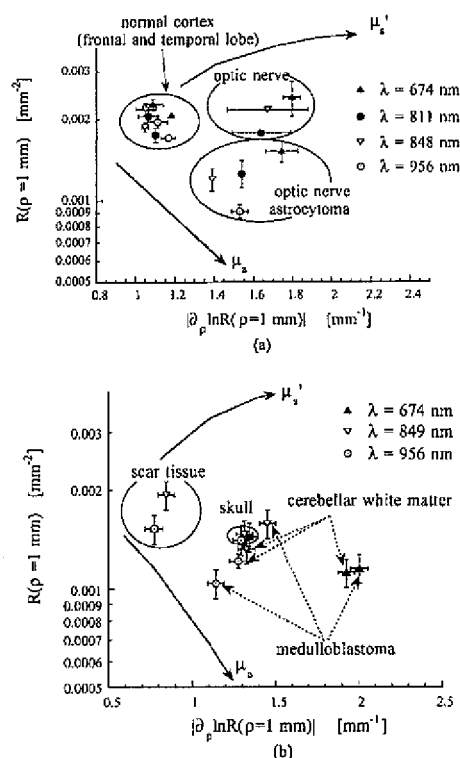
Fig. 11. Clinical measurements *in vivo* on human brain for (a) case 1 and (b) case 2. Plot of $R(\rho = 1)$ and $|\partial_\rho \ln R(\rho = 1 \text{ mm})|$ for different types of brain tissue: (a) normal cortex (frontal and temporal lobe), optic nerve astrocytoma, and normal optic nerve; (b) skull, deep cerebellar white matter with scar tissue, medulloblastoma, and deep cerebellar white matter (surrounding normal tissue).

error of the absolute value of $\mu_s'$ is estimated to be 5%.

In some cases, as shown, for example, in Fig. 12, the nearest fiber does not perfectly fit the simulation. Different reasons may be suggested. First, this fiber is at the limit of the region where only the parameter $\gamma$ must be taken into account. Therefore higher moments of the phase function may also be considered. Second, this fiber probes the tissue more superficially than the other fibers (see Fig. 5), and the differences that occur at the nearest fiber may be due also to tissue heterogeneity.

As reported in Table 1, with the exception of the normal optic nerve, the absorption coefficients at 811 and 849 nm are lower than those obtained at $\lambda = 674$ nm or $\lambda = 956$ nm. This result is consistent with the fact that the main near-IR tissue chromophores, hemoglobin and water, have an absorption maximum at approximately $\lambda < 700$ nm and $\lambda = 970$ nm, respectively.[31] The overall absorption is much higher in the tumor than the cortex presumably because of the greater hemoglobin in the tumor. Tumors generally grow more new blood vessels and thus have a higher hemoglobin concentration.

The $\mu_s'$ of the tumor is similar to the cortex at $\lambda = 956$ nm. However, the variation of $\mu_s'$ between $\lambda = 674$ nm and $\lambda = 956$ nm is much larger for the tumor than for the cortex: $\Delta\mu_s' \approx 0.57$ mm$^{-1}$ for tumor and $\Delta\mu_s' \approx 0.10$ mm$^{-1}$ for the cortex. Such spectroscopic variations may be attributable to structural differences between tissue types. Indeed such differences may depend on the average size or size distribution of scattering structures within or between cells.

Higher scattering is found for the normal optic nerve compared with all the other tissues in case 1. This is likely due to the presence of myelin. *In vitro* measurements have also shown that myelin containing white matter exhibits a higher scattering coeffi-

to almost identical $\mu_s'$ (differences of less than 5%) and an overestimation of $\mu_a$ of ~0.02 mm$^{-1}$. Taking into account the uncertainties of the measurements [~5% on $R(\rho = 1$ mm) and $|\partial_\rho \ln R(\rho = 1$ mm)$|$ for this tissue] and the uncertainty of $\gamma$ ($\pm 0.2$), the

Table 1. Optical Properties of Normal and Malignant Human Brain Tissue, Case 1

| Type of Tissue | Wavelength (nm) | Probe Measurements | | | FDPM[a] | |
|---|---|---|---|---|---|---|
| | | $\gamma$ | $\mu_s'$ (mm$^{-1}$) | $\mu_a$ (mm$^{-1}$) | $\mu_s'$ (mm$^{-1}$) | $\mu_a$ (mm$^{-1}$) |
| Cortex (frontal lobe) | 674 | $1.9 \pm 0.2$ | $1.00 \pm 0.05$ | $<0.02 \pm 0.01$ | 1.12 | 0.0173 |
| | 811 | $1.9 \pm 0.2$ | $0.91 \pm 0.05$ | $<0.01 \pm 0.01$ | 0.74 | 0.0182 |
| | 849 | $1.9 \pm 0.2$ | $0.92 \pm 0.05$ | $<0.01 \pm 0.01$ | 0.74 | 0.0185 |
| | 956 | $1.9 \pm 0.2$ | $0.89 \pm 0.05$ | $0.015 \pm 0.01$ | 0.80 | 0.0206 |
| Cortex (temporal lobe) | 674 | $1.9 \pm 0.2$ | $1.00 \pm 0.05$ | $0.02 \pm 0.01$ | 0.99 | 0.0179 |
| | 811 | $1.9 \pm 0.2$ | $0.82 \pm 0.05$ | $0.02 \pm 0.01$ | 0.48 | 0.0190 |
| | 849 | $1.9 \pm 0.2$ | $0.82 \pm 0.05$ | $<0.01 \pm 0.01$ | 0.45 | 0.0179 |
| | 956 | $1.9 \pm 0.2$ | $0.82 \pm 0.05$ | $0.025 \pm 0.01$ | 0.42 | 0.0218 |
| Astrocytoma of optic nerve | 674 | $1.7 \pm 0.2$ | $1.25 \pm 0.10$ | $0.14 \pm 0.03$ | 0.92 | 0.0165 |
| | 811 | $1.7 \pm 0.2$ | $0.95 \pm 0.10$ | $0.12 \pm 0.03$ | 0.55 | 0.0190 |
| | 849 | $1.7 \pm 0.2$ | $0.76 \pm 0.10$ | $0.09 \pm 0.03$ | 0.59 | 0.0191 |
| | 956 | $1.7 \pm 0.2$ | $0.73 \pm 0.10$ | $0.15 \pm 0.03$ | 0.58 | 0.0323 |
| Normal optic nerve | 674 | $1.7 \pm 0.2$ | $1.75 \pm 0.20$ | $0.06 \pm 0.03$ | N/A | N/A |
| | 811 | $1.7 \pm 0.2$ | N/A | N/A | N/A | N/A |
| | 849 | $1.7 \pm 0.2$ | $1.60 \pm 0.20$ | $0.08 \pm 0.03$ | N/A | N/A |
| | 956 | $1.7 \pm 0.2$ | $1.52 \pm 0.20$ | $0.07 \pm 0.03$ | N/A | N/A |

[a]The uncertainty of the FDPM values, given by the fitting procedure (see Refs. 2 and 3), is typically 2%.

**Table 2. Optical Properties of Normal and Malignant Human Brain Tissue, Case 2**

| Type of Tissues | Wavelength (nm) | Probe Measurements | | | FDPM* | |
| --- | --- | --- | --- | --- | --- | --- |
| | | $\gamma$ | $\mu_s'$ (mm$^{-1}$) | $\mu_a$ (mm$^{-1}$) | $\mu_s'$ (mm$^{-1}$) | $\mu_a$ (mm$^{-1}$) |
| Skull | 674 | $1.9 \pm 0.2$ | $0.9 \pm 0.1$ | $0.05 \pm 0.02$ | 1.19 | 0.0208 |
| | 849 | $1.9 \pm 0.2$ | $0.9 \pm 0.1$ | $0.05 \pm 0.02$ | 0.91 | 0.0215 |
| | 956 | $1.9 \pm 0.2$ | $0.85 \pm 0.1$ | $0.05 \pm 0.02$ | 0.77 | 0.0355 |
| Cerebellar white matter | 674 | $1.9 \pm 0.2$ | $1.35 \pm 0.1$ | $0.25 \pm 0.05$ | 1.34 | 0.0165 |
| | 849 | $1.9 \pm 0.2$ | $0.85 \pm 0.1$ | $0.095 \pm 0.02$ | 0.98 | 0.0132 |
| | 956 | $1.9 \pm 0.2$ | $0.78 \pm 0.1$ | $0.090 \pm 0.02$ | 0.84 | 0.0299 |
| Medulloblastoma | 674 | $1.9 \pm 0.2$ | $1.40 \pm 0.1$ | $0.26 \pm 0.05$ | 1.05 | 0.0120 |
| | 849 | $1.9 \pm 0.2$ | $1.07 \pm 0.1$ | $0.10 \pm 0.02$ | 0.66 | 0.0079 |
| | 956 | $1.9 \pm 0.2$ | $0.4 \pm 0.1$ | $0.075 \pm 0.02$ | 0.54 | 0.0239 |
| Cerebellar white matter with scar tissues | 674 | $2.2 \pm 0.2$ | $0.65 \pm 0.05$ | $<0.02$ | N/A | N/A |
| | 849 | $2.2 \pm 0.2$ | $0.80 \pm 0.05$ | $<0.02$ | N/A | N/A |
| | 956 | $2.2 \pm 0.2$ | $0.65 \pm 0.05$ | $<0.02$ | N/A | N/A |

*The uncertainty of the FDPM values, given by the fitting procedure (see Refs. 2 and 3), is typically 2.5%.

cient compared with other tissue.[12,19,23] The accuracy of the measurement on the optic nerve tissue can be affected by the high anisotropy of this type of tissue. Indeed it has been reported that light propagation depends on whether the direction considered is parallel or perpendicular to the nerve fibers.[32–34] Interestingly, comparison between measurements with the two symmetric sources reveals larger differences than for the other tissues. This variation is represented in Fig. 11(a) by the relatively large uncertainties associated with the optic nerve measurements.

In case 2 the first measurements were acquired directly from the skull. The difference in reduced scattering properties between $\lambda = 674$ and 956 nm is very small ($\mu_s' = 0.9$ and 0.85 mm$^{-1}$, respectively) as shown in Fig. 11(b). Previously determined *in vitro* values[35] for pig skull were approximately twice as large. Such differences may be due to variations in water content and sample preparation between *in vivo* and *in vitro* studies.

Case 2 data were also obtained from in series deep cerebellar white matter with scar tissue, tumor (medulloblastoma), and cerebellar white matter in the excavated tumor bed. Figure 11(b) shows that scar



Fig. 12. Comparison between the spatially resolved reflectance curve measured *in vivo* on normal cortex (temporal lobe) and simulations.

tissue is well differentiated from other structures and is characterized by a high $\gamma$ value ($\gamma = 2.2$) and low absorption ($\mu_a < 0.02$ mm$^{-1}$), which is consistent with the low vascularization of such tissue. In contrast, larger $\mu_a$, smaller $\gamma$, and large spectroscopic differences in $\mu_s'$ are found in white matter and medulloblastoma. As in case 1 the large $\mu_a$ values obtained for the tumor can be related to higher hemoglobin content, as is often found for cancerous tissues. Taking into account measurement variability, no significant differences are found between the tumor and the surrounding normal white matter. However, it is not clear that the so-called normal tissue measured at the surgical boarder could be considered disease-free and unaffected by the tumor vasculature.

Some of the different types of tissue examined here showed a dependence on the phase-function parameter $\gamma$. This confirms that $\gamma$ may be a valuable parameter for tissue characterization. Nevertheless an improvement in the accuracy of the $\gamma$ determination would be necessary to conclude the importance of this parameter.

The optical coefficients that we obtained can be compared with measurements performed simultaneously with the FDPM technique. One should keep in mind that the depth investigated by the FDPM technique is greater compared with the spatially resolved technique described here. Generally the $\mu_s'$ values are similar between the two methods, whereas more differences are found for $\mu_a$. For the cortex and the skull measurements both $\mu_s'$ and $\mu_a$ values are generally in good agreement. The decrease in $\mu_s'$ from $\lambda = 674$–956 nm is more pronounced in the FDPM data. In contrast, important differences are found for $\mu_a$ results where tumor values (astrocytoma and medulloblastoma) obtained by FDPM are significantly lower. This can be explained by the sensitivity of the spatially resolved probe to the high local hemoglobin content that can be resolved only by the small source–detector separations. In contrast the large source–detector sep-
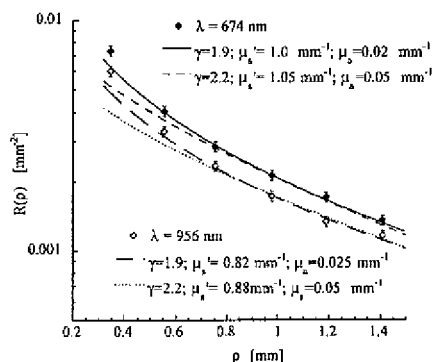
aration employed by the FDPM probe interrogates much greater larger-tissue volumes and hence measures average optical properties from multiple structures (e.g., normal + malignant).

## 4. Conclusions

The purpose of this research was to assess the performance of spatially resolved reflectance by using short source–detector separations (<1.4 mm). Monte Carlo simulations, the accuracy of which were confirmed by experiments on tissue phantoms, were used to establish the correspondence between the measured reflectance and the optical properties.

Optical properties that can be determined by this technique are the absorption coefficient $\mu_a$, the reduced scattering coefficient $\mu_s'$, and a parameter of the phase function $\gamma = (1 - g_2)/(1 - g_1)$, where $g_1(=g)$ and $g_2$ are the first and the second moment of the phase function. Experiments on calibrated Intralipid solutions and microsphere suspensions showed that changes in the absorption coefficient, reduced scattering coefficient, and $\gamma$ can be measured to within $\pm 0.005$ mm$^{-1}$, $\pm 0.05$ mm$^{-1}$, and $\pm 0.2$ respectively. Systematic errors are possible if the parameter $\gamma$ is not determined with sufficient accuracy. These performances could be improved by lowering the uncertainty on reflectance measurements.

Experiments and simulations helped to define the average volume probed by this technique. For typical tissues the average probe depth is typically ~1 mm and the influence of layers located below 3 mm is negligible.

Finally *in vivo* measurements on human brain showed that excellent discrimination can be obtained between different types of neural tissues, normal and abnormal. Good correlation has been found between spatially resolved reflectance and simultaneous measurements performed by FDPM. These two techniques offer interesting complementary features. The spatially resolved probe can potentially provide better differentiation between different types of tissue owing to its sensitivity to local structure, because substantially a smaller volume of tissue is probed. On the other hand, owing to physical limitations imposed by large near-IR mean absorption lengths in tissue, the precision for the $\mu_a$ estimate is likely to be worse. Consequently, the short distance, spatially resolved technique appears to be well suited for clinical settings that require rapid localized tissue identification, such as endoscopic or a needle-based optical biopsy, and intraoperative tissue mapping for surgical guidance.

## References and Notes

1. W.-F. Cheong, S. A. Prahl, and A. J. Welch, "A review of the optical properties of biological tissues," IEEE J. Quantum Electron. **26**, 2166–2185 (1990).
2. J. B. Fishkin, O. Coquoz, E. R. Anderson, M. Brenner, and B. J. Tromberg, "Frequency-domain photon migration measurements of normal and malignant tissue optical properties in a human subject," Appl. Opt. **36**, 10–20 (1997).
3. B. J. Tromberg, O. Coquoz, J. B. Fishkin, T. Pham, E. R. Anderson, J. Butler, M. Cahn, J. D. Gross, V. Venugopalan, and D. Pham, "Noninvasive measurements of breast tissue optical properties using frequency-domain photon migration," Philos. Trans. R. Soc. London Ser. B **352**, 661–668 (1997).
4. J. R. Mourant, I. J. Bigio, J. Boyer, R. L. Conn, T. Johnson, and T. Shimada, "Spectroscopic diagnosis of bladder cancer with elastic light scattering," Lasers Surg. Med. **17**, 350–357 (1995).
5. T. J. Farrell, M. S. Patterson, and B. C. Wilson, "A diffusion theory model of spatially resolved, steady-state diffuse reflectance for the noninvasive determination of tissue optical properties *in vivo*," Med. Phys. **19**, 879–888 (1992).
6. R. Bays, G. Wagnières, D. Robert, D. Braichotte, J.-F. Savary, P. Monnier, and H. van den Bergh, "Clinical determination of tissue optical properties by endoscopic spatially resolved reflectometry," Appl. Opt. **35**, 1756–1766 (1996).
7. A. Kienle, L. Lilge, M. S. Patterson, R. Hibst, R. Steiner, and B. C. Wilson, "Spatially resolved absolute diffuse reflectance measurements for noninvasive determination of the optical scattering and absorption coefficients of biological tissue," Appl. Opt. **35**, 2304–2314 (1996).
8. S. Fantini, M. A. Franceschini, J. B. Fishkin, B. Barbieri, and E. Gratton, "Quantitative determination of the absorption spectra of chromophores in strongly scattering media: a light-emitting-diode based technique," Appl. Opt. **33**, 5204–5213 (1994).
9. G. Mitic, J. Kölzer, J. Otto, E. Plies, G. Sölkner, and W. Zinth, "Time-gated transillumination of biological tissues and tissue-like phantoms," Appl. Opt. **33**, 6699–6710 (1994).
10. G. Kumar and J. M. Schmitt, "Optimal probe geometry for near-infrared spectroscopy of biological tissue," Appl. Opt. **36**, 2286–2293 (1997).
11. J. R. Mourant, I. J. Bigio, D. A. Jack, T. M. Johnson, and H. D. Miller, "Measuring absorption coefficients in small volumes of highly scattering media: source-detector separations for which path lengths do not depend on scattering properties," Appl. Opt. **36**, 5655–5661 (1997).
12. F. Bevilacqua, "Optical characterization of biological tissues *in vitro* and *in vivo*," Ph.D. dissertation 1781 (Swiss Federal Institute of Technology, Lausanne, 1998).
13. F. Bevilacqua and C. Depeursinge, "Monte Carlo study of diffuse reflectance at source–detector separations close to one transport mean free path," submitted to J. Opt. Soc. Am. A.
14. F. P. Bolin, L. E. Preuss, R. C. Taylor, and R. J. Ference, "Refractive index of some mammalian tissues using a fiber optic cladding method," Appl. Opt. **28**, 2297–2303 (1989).
15. D. R. Wyman, M. S. Patterson, and B. C. Wilson, "Similarity relations for anisotropic scattering in Monte Carlo simulations of deeply penetrating neutral particles," J. Comput. Phys. **81**, 137–150 (1989).
16. H. C. van de Hulst, *Multiple Light Scattering, Tables, Formulas, and Applications* (Academic, London, 1980).
17. S. L. Jacques, C. A. Alter, and S. A. Prahl, "Angular depen-

17. dance of HeNe laser light scattering by human dermis," Lasers Life Sci. **1**, 309–333 (1987).

18. R. Marchesini, A. Bertoni, S. Andreola, E. Melloni, and A. E. Sichirollo, "Extinction and absorption coefficients and scattering phase functions of human tissues *in vitro*," Appl. Opt. **28**, 2318–2324 (1989).

19. P. van der Zee, M. Essenpreis, and D. T. Delpy, "Optical properties of brain tissue," in *Photon Migration and Imaging in Random Media and Tissues*, B. Chance and R. R. Alfano, eds., Proc. SPIE **1888**, 454–465 (1993).

20. S. T. Flock, B. C. Wilson, and M. S. Patterson, "Total attenuation coefficient and scattering phase functions of tissues and phantom materials at 633 nm," Med. Phys. **14**, 835–841 (1987).

21. R. Graaff, A. C. M. Dassel, M. H. Koelink, F. F. M. de Mul, J. G. Aarnoudse, and W. G. Zijlstra, "Optical properties of human dermis *in vitro* and *in vivo*," Appl. Opt. **32**, 435–447 (1993).

22. P. Marquet, F. Bevilacqua, C. Depeursinge, and E. B. de Haller, "Determination of reduced scattering and absorption coefficients by a single charge-coupled-device array measurement, part I: comparison between experiments and simulations," Opt. Eng. **34**, 2055–2063 (1995).

23. F. Bevilacqua, P. Marquet, C. Depeursinge, and E. B. de Haller, "Determination of reduced scattering and absorption coefficients by a single charge-coupled-device array measurement, part II: measurements on biological tissues," Opt. Eng. **34**, 2064–2069 (1995).

24. G. H. Weiss, R. Nossal, and R. F. Bonner, "Statistics of penetration depth of photons reemitted from irradiated tissue," J. Mod. Opt. **36**, 349–359 (1989).

25. C. F. Bohren and D. R. Huffman, *Absorption and Scattering of Light by Small Particles* (Wiley, New York, 1983).

26. J. R. A. Bolt and J. J. ten Bosch, "Method for measuring position-dependent volume reflection," Appl. Opt. **32**, 4641–4645 (1993).

27. H. J. van Staveren, C. J. M. Moes, J. van Marle, S. A. Prahl, and Martin J. C. van Gemert, "Light scattering in Intralipid-10% in the wavelength range of 400–1100 nm," Appl. Opt. **30**, 4507–4514 (1991).

28. S. J. Madsen, B. C. Wilson, M. S. Patterson, Y. D. Park, S. L. Jacques, and Y. Hefetz, "Experimental tests of a simple diffusion model for the estimation of scattering and absorption coefficients of turbid media from time-resolved diffuse reflectance measurements," Appl. Opt. **31**, 3509–3517 (1992).

29. F. Bevilacqua, P. Marquet, O. Coquoz, and C. Depeursinge, "Role of tissue structure in photon migration through breast tissues," Appl. Opt. **36**, 44–51 (1997).

30. Protocol and informed consent were obtained from the patient undergoing neurological surgery for an intra-axial brain tumor as demonstrated on conventional neuroimaging. The protocol and informed consent documents were approved by the University of California Irvine review board (HS 96-495).

31. M Cope, "The development of a near infrared spectroscopy system and its application for noninvasive monitoring of cerebral blood and tissue oxygenation in the newborn infant," Ph.D. dissertation (University College London, London, 1991).

32. K. M. Hebeda, T. Menovsky, J. F. Beek, J. G. Wolbers, and M. J. C. van Gemert, "Light propagation in the brain depends on nerve fiber orientation," Neurosurgery, **35**, 720–722 (1994).

33. D. R. Sandeman, T. Mills, and S. G. Bown, "Enhancement of light penetration by white matter tracts in the normal mouse brain," Lasers Med. Sci. **3**, 47 (1986).

34. J. G. Wolbers, W. Kamphorst, H. J. M. Sterenborg, M. J. C. van Gemert, and W. Hogervorst, "Dose response of rat brains interstitially irradiated by argon light," Lasers Med. Sci. **2**, 255–260 (1987).

35. M. Firbank, M. Hiraoka, M. Essenpreis, and D. T. Delpy, "Measurements of the optical properties of the skull in the wavelength range 650–950 nm," Phy. Med. Biol. **38**, 503–510 (1993).

# A Theoretical Study of the Signal Contribution of Regions of the Adult Head to Near-Infrared Spectroscopy Studies of Visual Evoked Responses

Michael Firbank, Eiji Okada,* and David T. Delpy†,[1]

*University Department of Radiology, Imaging Laboratory, Royal Victoria Infirmary, Newcastle upon Tyne, NE1 4LP, United Kingdom;*
*†Department of Medical Physics and Bioengineering, University College London, 11-20 Capper Street, London WC1E 6JA, United Kingdom;*
*and *Department of Electronics and Electrical Engineering, Keio University, 3-14-1, Hiyoshi, Kohoku-ku, Yokohama 223 Japan*

Near-infrared (NIR) spectroscopy has been used in studies of the cerebral hemodynamic response to visual processing. In this paper, we present theoretical results from finite element and Monte Carlo modeling in order to help understand the contribution to the NIR signal from different parts of the head. The results from the models show that at the typical optode spacings used in these studies, an infrared spectroscopy measurement of *intensity* is sensitive to the outer 1–2 mm of the cortical gray matter and the partial optical path length in the gray matter is approximately 10 mm, compared with a total optical path length of 400 mm. When the NIR measurement is of *change in mean photon arrival time* (or *phase shift*), the signal comes from the upper 2–4 mm of the cortical surface and there is an increased lateral spread of the contributing tissue. We predict that for a 4-cm separation of input and detection optodes at 800 nm, a 1 µM change in hemoglobin concentration in the cortex corresponds to an attenuation change of approximately 0.001 OD (optical density) or 1 ps mean time change. Movement of the brain caused by this increase in volume will cause an absorption change of approximately half this magnitude, but does not affect the photon arrival time at 4-cm spacing. A discrepancy between the predicted and the experimentally measured intensities may support the supposition that the NIR signal is actually very sensitive to changes occurring in the pial cerebral vessels lying on the brain surface.    1998 Academic Press

## INTRODUCTION

Near-infrared (NIR) spectroscopy can be used to noninvasively monitor variations in cerebral blood oxygenation by measuring changes in the attenuation of NIR light passing through tissue (Jöbsis, 1977; Ed-

wards *et al.*, 1988; Hampson and Piantadosi, 1988; Wyatt *et al.*, 1990; De Blasi *et al.*, 1993; Elwell *et al.*, 1994). To carry out a study, near-infrared light is transported to the head by optical fibers which are usually terminated with reflective prisms (henceforth called optodes) which direct the light into the tissues. Light is collected by a similar fiber arrangement and detected by a photomultiplier tube or photodiode. The separation between input and detection optodes is usually in the range 2–4 cm. Changes in optical attenuation are then measured at a number of wavelengths, and these can be related to changes in hemoglobin oxygenation and concentration using the known absorption spectra of the hemoglobin (Wray *et al.*, 1988). Measurements can also be made of time of flight of the light or the phase shift of intensity modulated light. A review of the different measurement types used in NIR spectroscopy can be found in Delpy and Cope (1997).

Recently, several authors (Hoshi and Tamura, 1993; Villringer *et al.*, 1993; Maki *et al.*, 1995; Meek *et al.*, 1995; Gratton *et al.*, 1995a) reported studies using NIR spectroscopy to investigate the response of the brain to visual or motor stimuli. For these studies, the optodes are placed on the scalp over the appropriate cortical area, a suitable stimulus protocol is followed, and changes in hemoglobin oxygenation and concentration are followed. One study (Gratton *et al.*, 1995b) also reported light-scattering changes in the tissues. Usually, the stimulus is repeated several times with a rest period between, and, if necessary, the measurements are averaged over the stimulus cycle.

At present, the interpretation of the measured attenuation is limited by incomplete knowledge of which regions in the brain are being sampled by the NIR light, although some attempts to define the region have been made by comparing NIRS data with that obtained from PET (Hoshi *et al.*, 1994; Hock *et al.*, 1997) and fMRI studies (Kleinschmidt *et al.*, 1996). Developments of mathematical models of light propagation are ongoing,

---

[1] To whom correspondence should be addressed.

and recent theoretical modeling (Okada *et al.*, 1997; Firbank *et al.*, 1996; Hielscher *et al.*, 1997) has indicated that the path taken by the light is greatly affected by the CSF, particularly in the adult head. The CSF is a clear fluid which cannot be modeled by simple diffusion theory approximations of light transport. Results from the more recent modeling, which can correctly incorporate the effects of the CSF, indicate that the light penetration in the adult brain may be limited to the outer cortical gray matter (Firbank *et al.*, 1996; Okada *et al.*, 1996, 1997).

The purpose of this investigation, therefore, was to model the distribution of light in the brain in a visual evoked-response study and to predict what proportion of the detected signal arises from cerebral tissue in order to help in the interpretation of experimentally measured changes in optical attenuation.

## THEORETICAL BASIS OF OPTICAL SPECTROSCOPY *IN VIVO*

In a clear solution, light attenuation is linearly related to the compound concentration, its specific absorption coefficient, and the distance traveled through the solution. This is known as Beer's law. For a clear solution with absorption coefficient $\mu_a$ in a cuvette of thickness $d$, the attenuation $A$ is given by

$$A = \ln (I_0/I) = \mu_a d, \tag{1}$$

where $I_0$ is the incident intensity and $I$ the measured intensity. For a scattering medium, the distance the light travels is greater than the physical distance between the source and the detector, but it has been shown (Delpy *et al.*, 1988) that Eq. (1) can still be used to relate *changes* in absorption ($\Delta\mu_a$) to *changes* in attenuation ($\Delta A$), provided that the mean distance, $L$, traveled by the light is known,

$$\Delta A = \ln (I_1/I_2) = \Delta\mu_a L, \tag{2}$$

where $I_1$ and $I_2$ are the intensities measured, and the mean distance

$$L = \beta d, \tag{3}$$

$\beta$ being a numerical factor representing the increase in path traveled by the light due to multiple scattering.

Obviously, Eq. (2) can be rewritten in terms of the optical pathlength:

$$L = \frac{\Delta A}{\Delta\mu_a}. \tag{4}$$

This equation can be used to calculate the optical pathlength $L$ in a homogeneous medium from the change in attenuation due to a small change in absorption coefficient. In the case of a heterogeneous medium, where the absorption can change differently in different regions, the partial path length can be defined for a change in region $x$:

$$L(x) = \frac{\Delta A}{\Delta\mu_a(x)}. \tag{5}$$

Since experimentally it is not possible to vary the absorption coefficient of tissues in a controlled manner, it is not possible to measure the partial path length of different regions of the head *in vivo*. Measurements in phantoms are possible, however, as are calculations of the partial path length from accurate mathematical models of light transport.

One implication of the above equation is that if a change in absorption (i.e., chromophore concentration) occurs in one region only, the change in $\mu_a$ (and hence concentration) can only be calculated if the partial path length in that region is known.

### Photon Measurement Density Functions (PMDFs)

The PMDF describes how sensitive a measurement is to different points in the tissue. Two types of measurement are considered in this paper: simple attenuation changes, from which concentration changes can be derived as described above, and mean time measurements. The latter is a measurement of the average time taken by light to travel from the source to the detector optode. Obviously, this is equivalent to the mean distance traveled divided by the speed of light. Mean time can be measured either by timing ultrashort pulses of light as they pass through the tissue or by using amplitude-modulated light, in which case the phase shift of the detected light is measured. In tissue, mean time $\langle t \rangle$ and phase shift $\phi$ (in radians) are simply related by

$$\langle t \rangle = \frac{\phi}{2\pi f}, \tag{6}$$

provided that the modulation frequency, $f$, is less than 200 MHz (Arridge *et al.*, 1992).

The mean time (or phase shift) can be used as an *in vivo* measurement of total path length. Changes in $\mu_a$ and scattering coefficient ($\mu_s$) will cause changes in it, as well as changing attenuation. Gratton *et al.* (1995b) reported fast changes (100–200 ms) in the phase shift during an evoked-response study which they claim are caused by changes in scattering as the neurons depolarize following the stimulation.

FIG. 1. A MRI scan with manually generated outlines.

The calculation of PMDFs, which has usually been done with diffusion theory, is discussed elsewhere (Arridge, 1995; Arridge and Schweiger, 1995), but a brief definition is as follows.

For intensity measurements, the PMDF $J(p, m, s)$ at position $p$ in the tissue, for a source at $s$ and measurement of change in fluence $\Delta\Gamma(m)$ at position $m$, is

$$J_\Gamma(p, m, s) = \frac{\Delta\Gamma(m)}{\Delta\mu_a(p)}, \tag{7}$$

$\Delta\mu_a(p)$ being the change in absorption coefficient at $p$.

Similarly, for mean time $\langle t \rangle$, the corresponding PMDF is

$$J_{\langle t \rangle}(p, m, s) = \frac{\Delta\langle t \rangle(m)}{\Delta\mu_a(p)}. \tag{8}$$

Note that the mean time PMDF can be either positive or negative, since an increase in absorption coefficient can cause either an increase or decrease in mean time depending upon the position of the change relative to the source and detector optodes.

### Differential Mean Time Factor

To calculate the effect of absorption changes in a region on the mean time, we can define the differential mean time factor (DMTF) for region $x$ in a similar fashion to Eq. (5):

$$DMTF(x) = \frac{\Delta\langle t \rangle}{\Delta\mu_a(x)}. \tag{9}$$

### TECHNIQUES

A MRI scan of one of the authors' heads was taken and an axial slice through the region of the visual cortex selected. This image was used to generate outlines (Fig. 1) of the gray matter, white matter, CSF, and extra cerebral tissue (skull, skin). These outlines were used to generate a finite element mesh (see Fig. 2). The approximate radii of the tissue types were also measured and used in a separate cylindrical model of the tissues. The dimensions and tissue optical properties (absorption coefficient $\mu_a$ and transport scattering coefficient $\mu_s$) are shown in Table 1.

The optical properties are typical of those quoted in the literature (Firbank et al., 1993; van der Zee et al., 1993; Cheong, 1995) at 800 nm. Oxygenated and deoxygenated hemoglobin have an isobestic point at 798 nm, with an absorption coefficient of 0.2 mm$^{-1}$ mM (Matcher et al., 1995). All absorption and scattering coefficient are in base $e$.

Since diffusion theory is only valid in scattering regions, a hybrid diffusion/radiosity model was used to calculate light transport in the head. In this scheme, which has been specifically developed to cope with tissues containing clear regions (Firbank et al., 1996), a 2D finite element model (FEM) solution of the diffusion equation (Arridge et al., 1993) is used to calculate light transport in the scattering regions, while in the nonscattering regions of the CSF (the blank section in the middle of the mesh in Fig. 2), radiosity light tracing is employed. This hybrid scheme has been validated against both experimental measurements in phantoms and a Monte Carlo model (Firbank et al., 1996).

In addition, we performed a Monte Carlo simulation (Hiraoka et al., 1993) of a concentric cylinder with
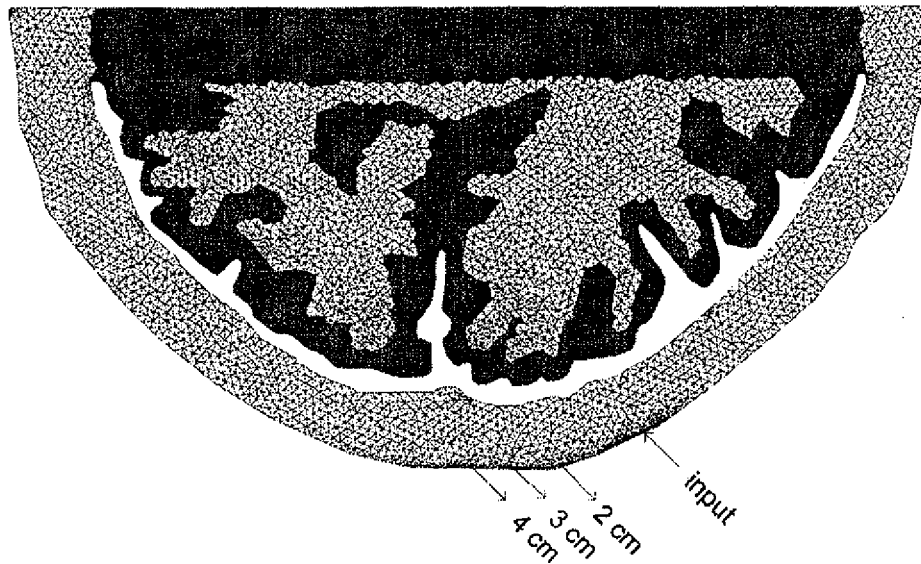
**FIG. 2.** Finite element mesh generated from Fig. 1.

properties as shown in Table 1, using 5 million input photons. This was a 3D simulation. FEM/radiosity calculations were also performed for a 2D cylindrical geometry.

The simplified cylindrical geometry was used in order to investigate the effect of changing the thickness of the CSF, since it is easier to define a thickness change for a uniform layer (in a previous study, we have shown that the presence of the sulci have little effect upon the thickness of the brain tissue contributing to the NIRS signal) (Okada *et al.,* 1997). The FEM model based upon the MRI data, however, allowed qualitative analysis of the effect of the nonuniformity of the gray matter surface. The 3D Monte Carlo cylinder model was run to investigate the spread of light perpendicular to the measurement plane, since this is not possible to do in a 2D model (which our finite element model is currently restricted to because of the computation time required).

PMDFs were generated with source/detector separations of 2, 3, and 4 cm which are typical of the values used in the published evoked-response studies. The input position for the light in the MRI generated geometry is shown in Fig. 2. This was chosen to be approximately over the visual cortex while avoiding the sagittal sinus. Data for the surface fluence and mean time were calculated at all detector positions.
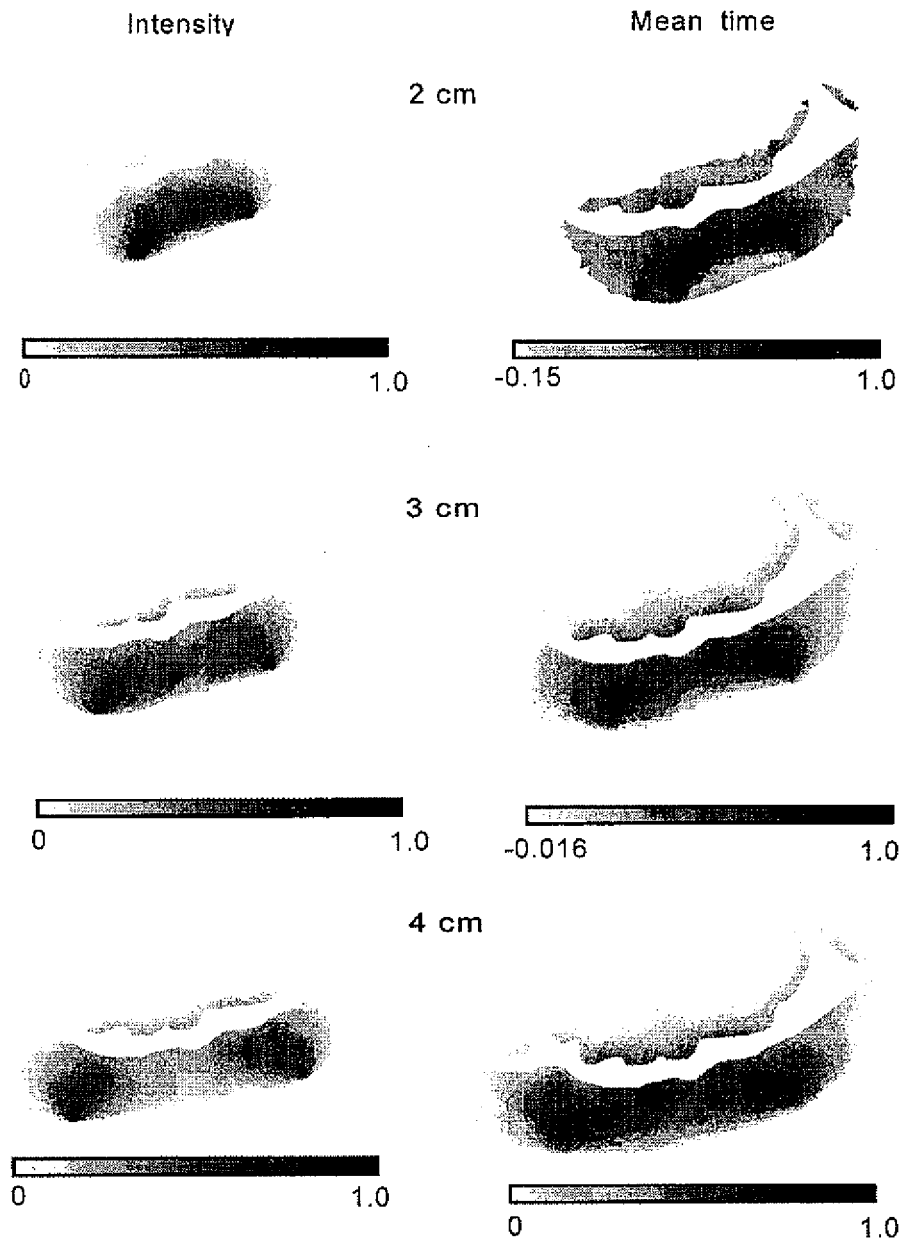
**RESULTS**

Figure 3 shows the PMDFs for measurements of mean time and intensity for the FEM calculations on the head. These show that for a measurement of *intensity,* the region of the brain which is interrogated is limited to the cortical gray matter immediately below and between the optodes and that this region is sampled approximately uniformly. For a measurement of *mean time* (or *phase* if using an intensity modulated spectrometer) a slightly greater region is sampled in terms of both depth and lateral spread. The depth of gray matter sampled does not increase substantially with increased optode spacing. Figures 4a and 4b show profiles of the PMDFs in the brain tissue halfway between the optodes and perpendicular to them (in the 2D plane) for source/detector spacings of 2, 3, and 4 cm. The profiles have been normalized by dividing each of them by the received signal at the appropriate spacing. The contribution of the tissue to the detected signal falls exponentially with distance into the gray matter; the $1/e$ penetration depth for the intensity PMDF in the gray matter can be calculated as 1.5 mm and for the mean time as 2.4 mm.

Figure 5a shows the optical path lengths in each of the tissue types as a function of optode spacing. This is proportional to the attenuation change caused by a variation in absorption within that region. A 1 µM increase in blood concentration in the skin will hence give rise to a change in attenuation approximately 20 times bigger than a 1 µM change in the gray matter. The partial path length through the white matter is less than 0.5 mm and is effectively zero on this scale, and hence changes in blood concentrations solely occurring there will not be seen.

**TABLE 1**

| Tissue | Radius (mm) | $\mu_a$ (mm$^{-1}$) | $\mu_s$ (mm$^{-1}$) |
| --- | --- | --- | --- |
| White matter | 68.5 | 0.005 | 6.0 |
| Gray matter | 75.5 | 0.025 | 2.5 |
| CSF | 79.0 | 0.003 | 0.001 |
| Skin/skull | 92.0 | 0.01 | 2.0 |

Intensity                                              Mean time

2 cm

0                           1.0        -0.15                      1.0

3 cm

0                           1.0        -0.016                     1.0

4 cm

0                           1.0

0                           1.0

**FIG. 3.**   Intensity and mean time PMDFs for 2-, 3-, and 4-cm optode separation. For the intensity PMDF, dark color indicates an increase in attenuation with increase in $\mu_a$. For the mean time PMDF, dark color indicates a decrease in mean time with increase in $\mu_a$ and light color an increase in mean time.

Figure 5b shows a similar graph for the mean time, the $y$ axis showing the change in mean time for a change in absorption coefficient. The mean time measurement is approximately twice as sensitive to changes occurring in the brain than the intensity measurement, although it still is a factor of 10 less than the surface regions.

Information about the spread of photons perpendicular to the source/detector plane was gained from the 3D concentric cylinder Monte Carlo model by recording the position of all detected photons as they passed through the surface of the gray matter. The resulting intensity

PMDFs are shown in Fig. 6. Figure 7 shows the profile through the PMDFs along the axis indicated by the dotted line normalized by the total detected intensity. As can be seen, the light probes an area of brain approximately 1 cm on either side of the source/detector plane. This vertical spread does not change significantly with source/detector spacing. It is worth noting that the use of a cylindrical as opposed to a spherical 3D model would, if anything, slightly overestimate the vertical spread to be expected, so the values presented here probably represent a maximum extent to the sampled tissue volume (Okada *et al.,* 1996, 1997).
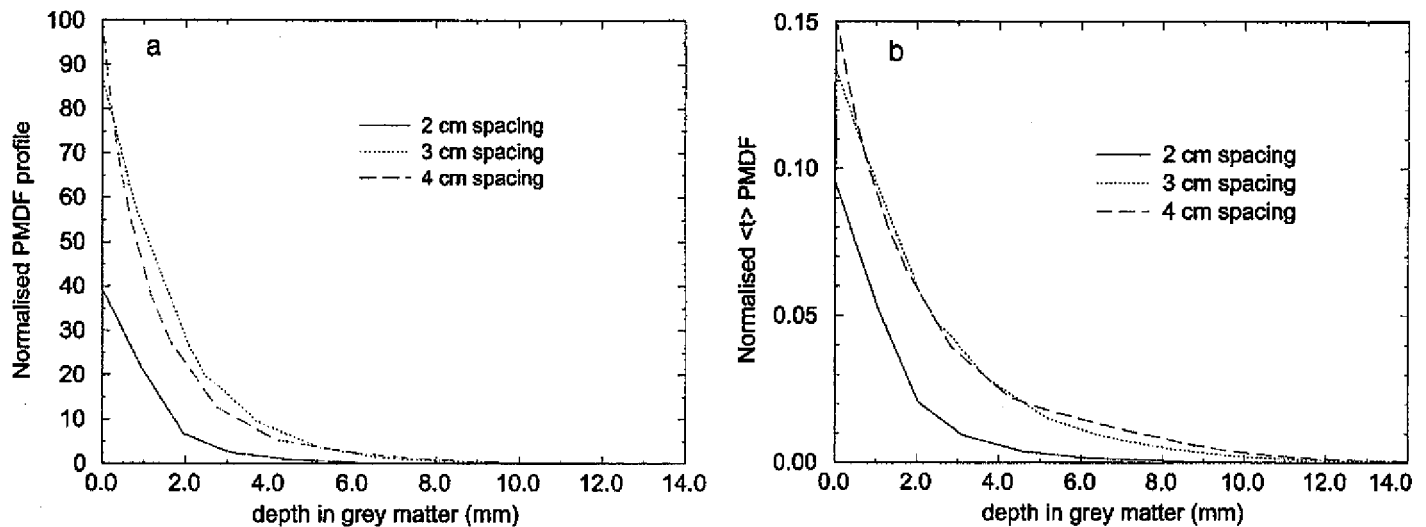
**FIG. 4.** Profile through (a) intensity and (b) mean time PMDFs in gray matter for 2-, 3-, and 4-cm optode separation for the FEM/radiosity calculation on the MRI-generated mesh.

## Effect of Brain Movement

In NIRS studies, optical changes can be observed in synchrony with both the heart and the respiratory rates, and these need to be filtered out in measuring the small evoked-response signal (Gratton and Corballis, 1995). These signals have usually been assumed to be due to changes in blood flow/volume that occur with each heart beat or respiration (Elwell *et al.,* 1994), but it is also possible that they can arise due to movements of the brain surface or from pial cerebral vessels lying on the brain surface. The brain is not fixed inside the skull and can move or expand to a limited degree. The pulsatile nature of the blood flow causes the brain to

throb with the heart beat. This has been observed in patients undergoing brain surgery, although in NIR studies, of course, the skull is not opened, and the brain has less room for movement.

Changes in the blood volume of the brain (as part of an evoked response) will also lead to a change in brain volume and will cause it to expand or shrink, displacing CSF. Both the absorption and the volume change may alter the light distribution in the head, resulting in an optically observable signal. We have applied our previously described modeling to determine the relative contributions of movement and absorption variation to the NIRS signal.
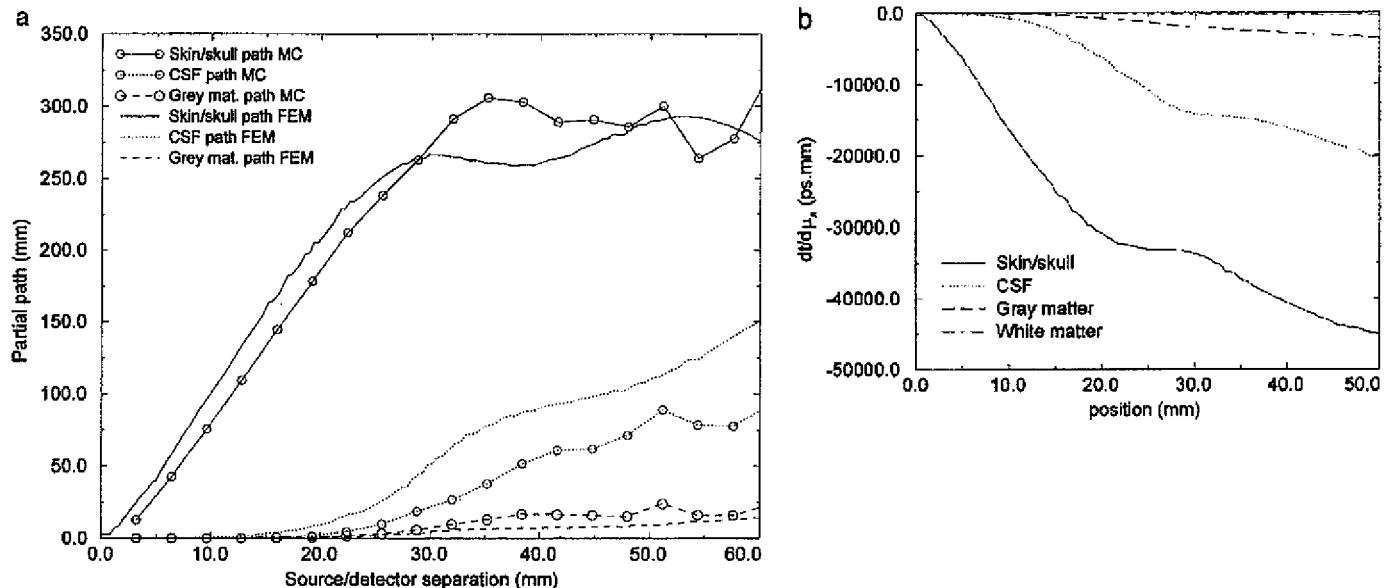


**FIG. 5.** (a) Partial path lengths though skin/skull, CSF, and gray matter for FEM/radiosity calculation on the MRI-generated mesh and Monte Carlo modeling of the 3D cylinder and (b) differential mean time factor for different regions for FEM/radiosity calculation on the MRI-generated mesh.
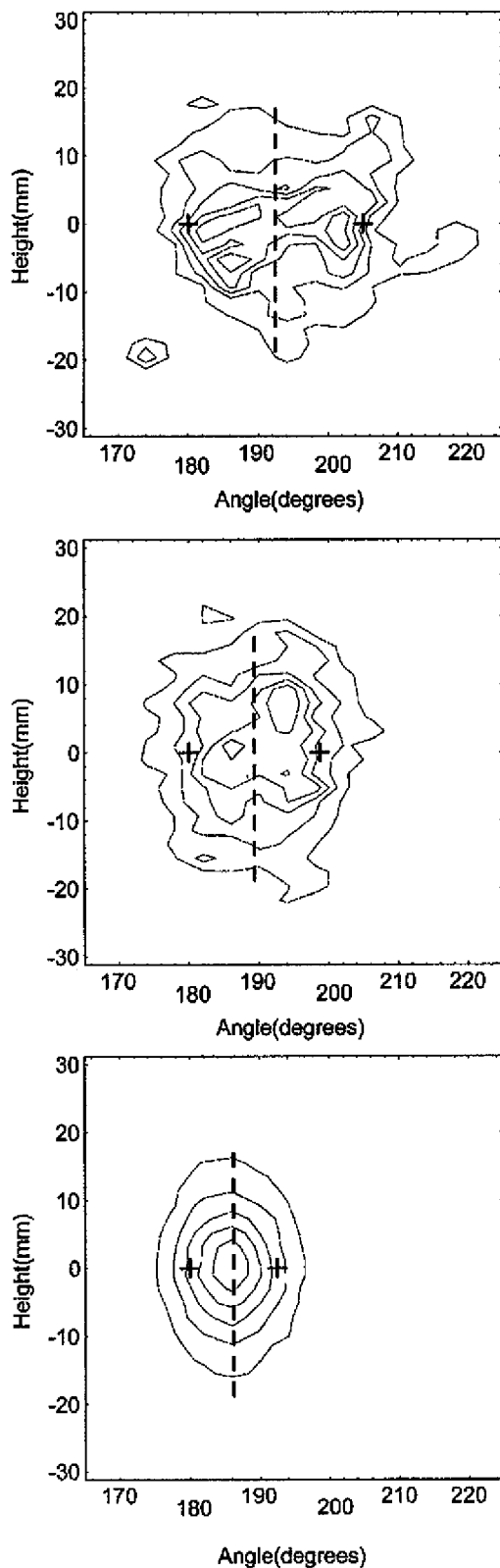
**FIG. 6.** Monte Carlo-generated intensity PMDFs for the gray matter/CSF interface, showing the vertical spread of the light on the gray matter surface. PMDFs are shown for light detected at 2-, 3-, and 4-cm separation. The positions of the optodes are shown with a cross. The dotted line shows the direction across which the profiles were generated (see Fig. 7).
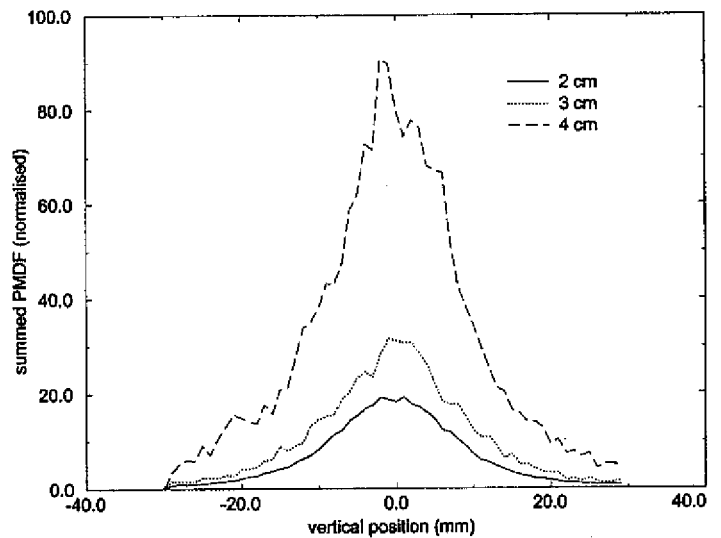


**FIG. 7.** Profile of detected photons as they cross the gray matter boundary for 2-, 3-, and 4-cm source/detector spacing.

Greitz *et al.* (1992) reported pulsatile brain movement using magnetic resonance phase imaging in adult volunteers. This movement was greatest around the base of the brain (0.1 mm displacement and velocities of up to 2 mm/s). The magnitude of the motion decreased toward the periphery of the brain, however, and was less than 0.01 mm at the brain surface.

Figure 8 shows the calculated change in attenuation and mean time for a decrease of 0.1 mm of the CSF thickness in the simplified cylindrical model (i.e., the inner radius of the CSF changes from 75.5 to 75.6 mm, with all other parameters remaining constant).

When the blood volume in the brain increases, the attenuation will change for two reasons: (a) because the blood content has increased, causing higher absorption, and (b) because the brain will expand slightly, changing the distribution of light in the head. Figure 9 shows a
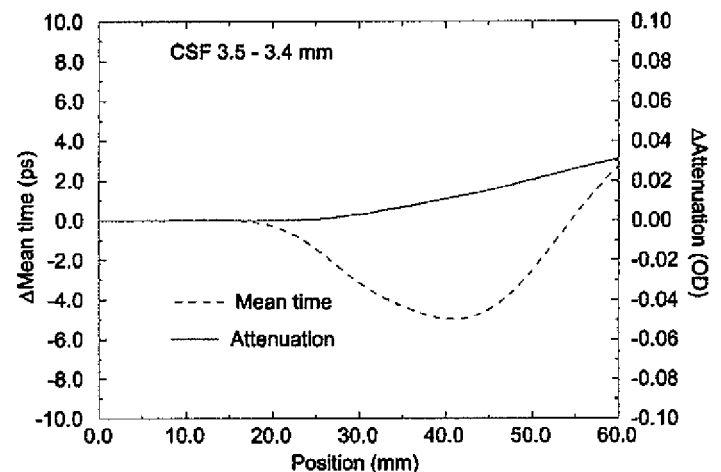


**FIG. 8.** Change in attenuation and mean time for CSF thickness decreasing from 3.5 to 3.4 mm (in 2D cylinder FEM/radiosity).
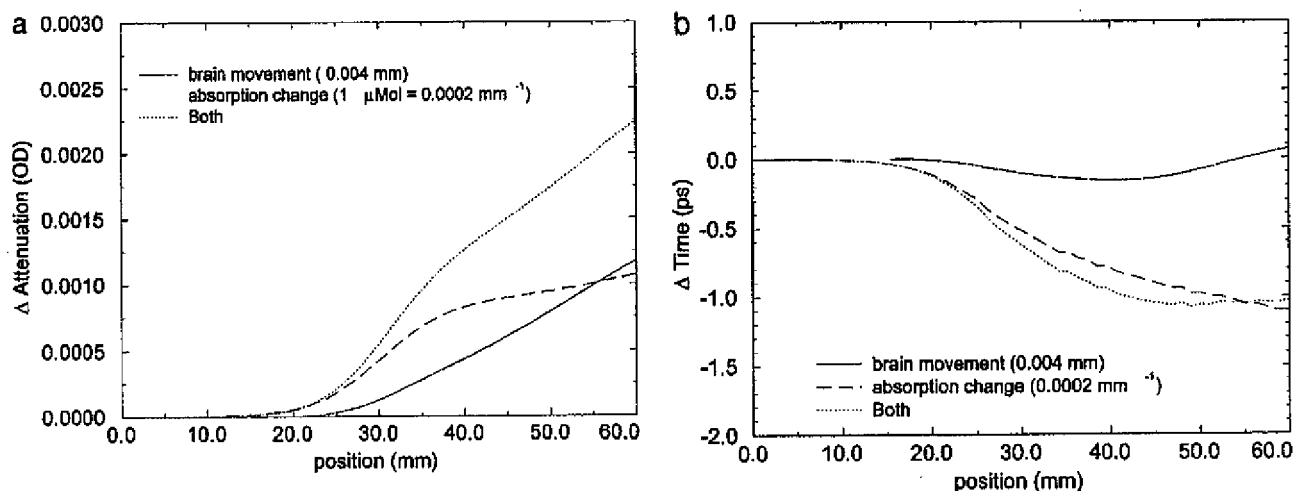
**FIG. 9.** Comparison of signal change for (a) attenuation and (b) mean time caused by an absorption increase with that caused by brain expansion due to increased blood volume (from 2D cylinder FEM/radiosity calculation).

comparison of these two effects, i.e., an increased absorption, but constant geometry, and an increased brain volume at constant absorption. The data are calculated for a 1 µM change of hemoglobin concentration in the gray matter. The gray matter thickness is 7 mm and the brain blood volume is approximately 5% with a typical hemoglobin concentration of 84 µM (Sakai et al., 1985), so a 1 µM increase is equivalent to $5 \times 1/84 = 0.06\%$ increase in volume and so assuming that the brain swells outward only and that the brain hematocrit stays constant, this is equivalent to an increase of 0.004 mm in thickness.

## IMPLICATIONS

When used on the scalp surface, NIR spectroscopy can pick up changes in hemoglobin concentration on the cortical surface. The signal is probably limited to changes in hemodynamics occurring in the top 2–3 mm of the cortex. The area of the brain surface which contributes to the signal is approximately as wide as the optode spacing and extends laterally 1 cm either side perpendicular to the optode position. In NIR spectroscopy, the calculated quantity $\Delta CL$ is a product of the changes in concentration and optical pathlength. To derive absolute changes in concentration, the optical path length must be known. If the concentration changes are limited to one region only, the partial path length in that region must be known to calculate the change in concentration correctly. In the case of evoked response studies, the hemoglobin concentration changes are assumed to occur in the brain only. Although the PMDFs are weighted toward surface tissues, this does not necessarily mean that NIRS signal comes mainly from the surface. This is because in evoked-response studies, we are measuring *changes* in signal, and if the

only change in hemodynamics occurs in the brain, then that is what will be detected. The technique is, however, more sensitive to changes occurring in the skin and skull than in the brain.

While the exact dependence of the NIR signal contribution in an individual study will depend upon the geometry and the exact optical properties, in our theoretical model, we found that a 1 µM change in blood concentration will give rise to approximately 0.001 OD change in attenuation at 4-cm spacing and approximately 1-ps change in mean time. Typical instrumental noise at 3-cm spacing in tissue is 0.001 OD for attenuation and 0.1° in phase (equal to 1.4 ps at 200 MHz). This typically gets a factor of 3 worse for every centimeter increase in optode spacing and is essentially limited by the detected intensity and the quantum efficiency of the detecting device. The signal can of course be improved by averaging and performing several studies on the same volunteer.

It is interesting to note that, although experimentally the NIRS signal changes measured over the visual cortex vary considerably in magnitude from subject to subject, the average level of intensity change (Meek et al., 1995) and phase change (Gratton et al., 1995a) observed is approximately five times greater than that predicted from this simple modeling in which the hemoglobin changes are assumed to occur only in the brain parenchyma. We have previously speculated (Okada et al., 1997, 1998) that the considerable time spent by the light in the clear CSF would lead to it contributing significantly to the NIRS signal were an absorption change to occur within it. In reality, the CSF layer comprises the subarachnoid space which includes pial cerebral vessels lying on the brain surface. Any small change in the hemoglobin concentration, oxygenation, or size of these vessels as a result of an evoked

response is likely therefore to be a major contributor to the experimentally observed signal. The current hybrid diffusion/radiosity model cannot deal with this geometry, but work is under way to modify it to enable the effect of discrete absorbers within the clear layer to be modeled.

## ACKNOWLEDGMENTS

## REFERENCES

Arridge, S. R. 1995. Photon measurement density functions. Part I: Analytical forms. *Appl. Opt.* **34**:7395–7409.

Arridge, S. R., and Schweiger, M. 1995. Photon measurement density functions. Part II: Finite element method calculations. *Appl. Opt.* **34**:8026–8037.

Arridge, S. R., Schweiger, M., Hiraoka, M., and Delpy, D. T. 1993. A finite element approach for modelling photon transport in tissue. *Med. Phys.* **20**(2):299–309.

Arridge, S. R., Cope, M., and Delpy, D. T. 1992. The theoretical basis for the determination of optical pathlengths in tissue: Temporal and frequency analysis. *Phys. Med. Biol.* **37**:1531–1560.

Cheong, W.-F. 1995. Summary of optical properties. In *Optical-Thermal Response of Laser-Irradiated Tissue* (A. J. Welch and M. J. C. van Gemert, Eds.), pp. 275–303. Plenum, New York.

De Blasi, R. A., Cope, M., Elwell, C. E., Safoue, F., and Ferrari, M. 1993. Noninvasive measurement of human forearm oxygen consumption by near infrared spectroscopy. *J. Appl. Physiol.* **67**:20–25.

Delpy, D. T., Cope, M., van der Zee, P., Arridge, S. R., Wray, S., and Wyatt, J. S. 1988. Estimation of optical pathlength through tissue from direct time of flight measurements. *Phys. Med. Biol.* **33**:1433–1442.

Delpy, D. T., and Cope, M. 1997. Quantification in tissue near infrared spectroscopy. *Philos. Trans. R. Soc. London B* **352**:649–659.

Edwards, A. D., Wyatt, J. S., Richardson, C. E., Delpy, D. T., Cope, M., and Reynolds, E. O. R. 1988. Cotside measurement of cerebral blood flow in ill newborn infants by near infrared spectroscopy. *Lancet* **2**:770–771.

Elwell, C. E., Cope, M., Edwards, A. D., Wyatt, J. S., Delpy, D. T., and Reynolds, E. O. R. 1994. Quantification of adult cerebral haemodynamics by near-infrared spectroscopy. *J. Appl. Physiol.* **77**:2753–2760.

Firbank, M., Arridge, S. R., Schweiger, M., and Delpy, D. T. 1996. An investigation of light transport through scattering bodies with non-scattering regions. *Phys. Med. Biol.* **41**:767–783.

Firbank, M., Hiraoka, M., Essenpreis, M., and Delpy, D. T. 1993. Measurement of the optical properties of skull in the wavelength range 650–950 nm. *Phys. Med. Biol.* **38**:503–510.

Gratton, G., Corballis, P. M. 1995. Removing the heart from the brain: Compensation for the pulsatile artifact in the photon migration signal. *Psychophysiology* **32**:292–299.

Gratton, G., Corballis, P., Cho, E., Fabiani, M., and Hood, D. C. 1995a. Shades of gray matter: Noninvasive optical images of human brain responses during visual stimulation. *Psychophysiology* **32**:505–509.

Gratton, G., Fabiani, M., Friedman, D., Franceschini, M. A., Fantini, S., Corballis, P., and Gratton, E. 1995b. Rapid changes of optical parameters in the human brain during a tapping task. *J. Cognit. Neurosci.* **7**(4):446–456.

Greitz, D., Wirestam, R., Franck, A., Nordell, B., Thomsen, C., and Ståhlberg. 1992. Pulsatile brain movement and associated hydrodynamics studied by magnetic resonance phase imaging: The Monro-Kellie doctrine revisited. *Neuroradiology* **34**:370–380.

Hielscher, A. H., Alcouffe, R. E., and Barbour, R. L. 1997. Transport and diffusion calculations on MRI generated data. *Proc. SPIE* **2979**:500–508.

Hiraoka, M., Firbank, M., Essenpreis, M., Cope, M., Arridge, S. R., van der Zee, P., and Delpy, D. T. 1993. A Monte Carlo investigation of optical pathlength in inhomogeneous tissue and its application to near infrared spectroscopy. *Phys. Med. Biol.* **38**:1859–1876.

Hock, C., Villringer, K., MullerSpahn, F., Wenzel, R., Heekeren, H., SchuhHofer, S., Hofmann, M., Minoshima, S., Schwaiger, M., Dirnagl, U., and Villringer, A. 1997. Decrease in parietal cerebral hemoglobin oxygenation during performance of a verbal fluency task in patients with Alzheimer's disease monitored by means of near-infrared spectroscopy (NIRS)—Correlation with simultaneous rCBF–PET measurements. *Brain Res.* **755**:293–303.

Hoshi, Y., and Tamura, M. 1993. Detection of dynamic changes in cerebral oxygenation coupled to neuronal function during mental work in man. *Neurosci. Lett.* **150**:5–8.

Hoshi, Y., Onoe, H., Watanabe, Y., Andersson, J., Bergström, Lilja, A., Langstöm, and Tamura, M. 1994. Non synchronous behaviour of neuronal activity, oxidative metabolism and blood supply during mental tasks in man. *Neurosci. Lett.* **172**:129–133.

Jöbsis, F. F. 1977. Noninvasive infrared monitoring of cerebral and myocardial oxygen sufficiency and circulatory parameters. *Science* **198**:1264–1267.

Kleinschmidt, A., Obrig, H., Requardt, M., Merboldt, K.-D., Dirnagl, U., Villringer, A., and Frahm, J. 1996. Simultaneous recording of cerebral blood oxygenation changes during human brain activation by magnetic resonance imaging and near infrared spectroscopy. *J. Cereb. Blood Flow Metab.* **16**:817–826.

Maki, A., Yamashita, Y., Ito, Y., Watanabe, E., Mayanagi, Y., and Koizumi, H. 1995. Spatial and temporal analysis of human motor activity using noninvasive NIR topography. *Med. Phys.* **22**(12):1997–2005.

Matcher, S. J., Elwell, C. E., Cooper, C. E., Cope, M., and Delpy, D. T. 1995. Performance comparison of several published tissue near-infrared spectroscopy algorithms. *Anal. Biochem.* **227**:54–68.

Meek, J. H., Elwell, C. E., Khan, M. J., Romata, J., Wyatt, J. S., Delpy, D. T., and Zeki, S. 1995. Regional changes in cerebral haemodynamics as a result of a visual stimulus measured by near infrared spectroscopy. *Proc. R. Soc. London B* **261**:351–356.

Okada, E., and Delpy, D. T. 1996. The effect of overlying tissue on NIR light propagation in neonatal brain. *OSA TOPS Adv. Opt. Imaging Photon Migrat.* **2**:338–343.

Okada, E., Firbank, M., Schweiger, M., Arridge, S. R., Cope, M., and Delpy, D. T. 1997. Theoretical and experimental investigation of near infrared light propagation in a model of the adult head. *Appl. Opt.* **36**:21–31.

Okada, E., Tanigawa, Y., Yamada, Y., Firbank, M., and Delpy, D. T. 1998. Investigation of the direct and indirect signal contribution of brain haematoma in near infrared spectroscopy. *OSA TOPS Adv. Opt. Imaging Photon Migrat.*, in press.

Sakai, F., Nakazawa, K., Tazaki, Y., Ishii, K., Hino, H., Igarashi, H., and Kanda, T. 1985. Regional cerebral blood volume and hematocrit measured in normal human volunteers by single photon emission computed tomography. *J. Cereb. Blood Flow Metab.* **5**:207–213.

van der Zee, P., Essenpreis, M., and Delpy, D. T. 1993. Optical properties of brain tissue. *Proc. SPIE* **1888**:454–465.

Villringer, A., Planck, J., Hock, C., Schleinkofer, L., and Dirnagl, U. 1993. Near infrared spectroscopy (NIRS) a new tool to study hemodynamic changes during activation of brain function in human adults. *Neurosci. Lett.* **154**:101–104.

Wray, S., Cope, M., Delpy, D. T., Wyatt, J. S., and Reynolds, E. O. R. 1988. Characterization of the near infrared absorption spectra of cytochrome aa3 and haemoglobin for the non invasive monitoring of cerebral oxygenation. *Biochim. Biophys. Acta* **933**:184–192.

Wyatt, J. S., Cope, M., Delpy, D. T., Richardson, C. E., Edwards, A. D., Wray, S., and Reynolds, E. O. R. 1990. Quantitation of cerebral blood volume in human infants by near infrared spectroscopy. *J. Appl. Physiol.* **68**:1086–1091.

# EXHIBIT B

# Experimental study of NIR transmittance of the human skull

Vladislav V. Lychagov[a], Valery V. Tuchin[a], Maxim A. Vilensky[a], Boris N. Reznik[b], Thomas Ichim[b], Luis De Taboada[c],

[a] Institute of Optics and Biophotonics, Saratov State University, 83, Astrakhanskaya str., 410012,
[b] BioRASI, USA
[c] Photothera Inc., USA,

## ABSTRACT

The results of measurements of transmittance of high power laser irradiation through skull bones and scalp are presented. Dependences of transmittance on sample thickness were received. Character of transmittance was investigated and characteristics of heterogeneity of the scattering structure of the skull bones are proposed. Besides that, variation of temperature of skull and scalp surfaces under exposure of high power laser irradiation during experiments was controlled. Experimental results were verified by Monte-Carlo simulations.

Keywords: transmittance, bone structure, laser therapy, Monte-Carlo simulation

## 1. INTRODUCTION

During the last years laser technique had found increasingly wide application in medicine. In addition to using of high-power lasers in surgery (laser scalpel) laser irradiation is widely used in therapy. There are a lot of fields of application of laser therapy, such as: cure of arthritis, oculars, cardiac, skins and blood diseases. The influence of different types of laser systems on different biological objects was investigated during this time.

Laser therapy at present is one of the most effective methods of treatment and prophylaxis of various diseases, primarily owing to possibility of fine adjustment of biological processes and noninvasive influence on structure of biological tissues. However, it is necessary to define properly radiation dose to avoid of negative thermal effect on biological tissues. As is well known, the power density of laser irradiation within the range of from 0.1 to 10 mW/cm2 is had the most effective influence to human tissues. The lower power density of laser irradiation could exert just stimulation therapy; the abnormal changes in tissues could happen using the high value of power density of laser irradiation.

One of the possible adaptations of this method is a therapy of stroke and infarcts. Accordingly, the main aim of our studies was estimation of a dose of laser irradiation transmitted through skull bones and scalp tissue and arrived at a brain. A lot of parameters are significant in this case such as wavelength and power of irradiation, geometry of a beam, and mode of irradiation (continues wave, pulsed beam). To understand the adaptation processes within bone tissue it is not only necessary to take into consideration bone density but also bone structure.

## 2. EXPERIMENTS

Experimental research was carried out with preparing bone tissue and skin of the head. The scheme of the experimental setup is presented in Figure 1a. Collimated, 810 nm, 1 Watt laser beam of approximately 30 mm in diameter was used as a light source.

CCD camera with necessary neutral filters was used for obtaining of a pattern of spatial distribution of transmitted irradiation.
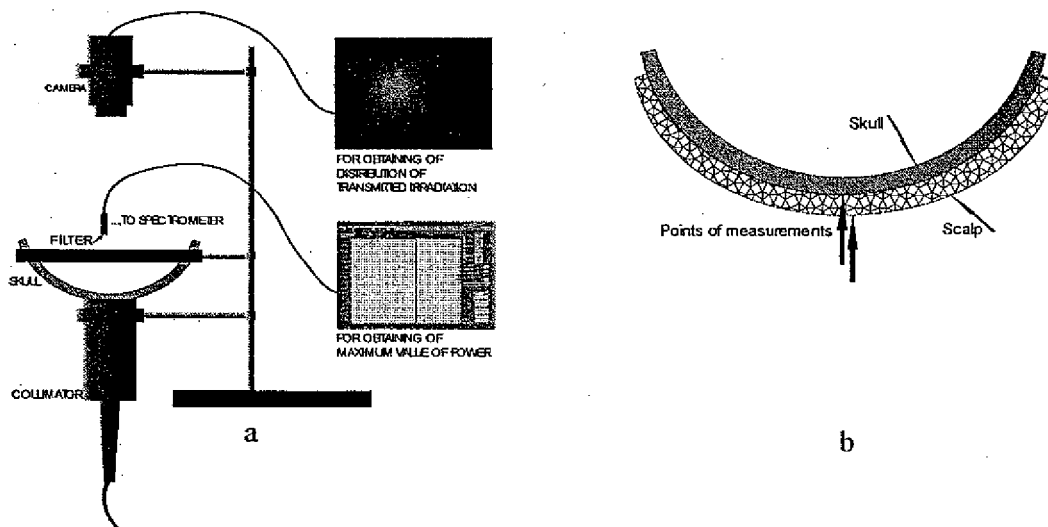
Figure 1: Experimental setup and method of measurements

The absolute value of power at the central of distribution (maximum power) was measured using a 1 mm diameter fiber with cosine corrector and an Ocean Optics a USB2000 spectrophotometer. Thickness of the sample was measured at five points with the help of the slide gauge and averaged. The skin samples were held between two object-plates during measurement. Temperature of samples was measured by the voltmeter V7-27A/1 with the contact probe for temperature detection (Fig. 1b). Square of working substance of the probe is equal to 1 square millimeter. Temperature was measured at the skin surface and skull in the center of irradiated field after exposure.

## 3. MEASUREMENTS

Using CCD we made a sequence of frames (25 frames) with each domain of interest (temples, forehead, occiput, and vertex) for averaging, sequence of frames with the laser switch off for subtraction of backgrounds, and one frame with the scale for calculation of real dimensions of the frames. Then maximum power in the center of the distribution was measured five times by the spectrometer, using available calibration, and the light distribution was normalized to mean value. The resulting power density distribution was calculated in the following way:

$$Pdistr_{res} = \left( \frac{Pdistr_1 + Pdistr_i + ... + Pdistr_{25}}{25} - \frac{Pbackgnd_1 + ... + Pbackgnd_{25}}{25} \right) \cdot \frac{(P\max 1 + ... + P\max 5)}{5 Pdistr\max}$$

The same procedure as described above was realized both with the skull only and with the skull with shaved scalp. After measurements we calculated the main characteristics of light transmittance: average radius of light distribution with the fixed power density, and its standard deviation. For example:

$$R_{0.7\max} = \frac{\sum\limits_{n=1}^{N} R_{An}}{N},$$

where $An$ is a point from vicinity of 0.7MaxPower level $(0.7-\varepsilon; 0.7+\varepsilon)$, and $R_{An}$ is a radius vector of this point on the assumption of $A0$ is a center of coordinate. $N$ – amount of this points. Analogously for $R_{0.5}$ and $R_{0.1}$.

## 4. RESULTS AND CONCLUSIONS

Measurements were carried out on 20 cadaver's heads, at 5 domains: forehead, left and right temples, occiput and vertex. In such a way dependence of transmittance on sample thickness was build up on 100 points. Measurements were performed both on the skull with shaved scalp and on the separate skull. In Figure 2 dependence of transmittance on sample thickness for both cases is presented.

As it can be seen from this picture, decrease of transmittance with increase of sample thickness can be approximated well by exponential decay. The value of transmittance is varied from 0.5% to 5% in case of sample with scalp and from 1% to 16% in case of single skull. In consequence of input power density was 68 mW/cm$^2$ value of transmitted power density varied from 340 $\mu$W/cm$^2$ to 3400 $\mu$W/cm$^2$ and from 680 $\mu$W/cm$^2$ to 9000 $\mu$W/cm$^2$ respectively. It is evident from results of experiments with separated bone tissue and experiments with skull and scalp, that layer of skin influences on transmittance the same way as skull, with that thickness of skin layer is less than thickness of skull. Such experimental results comply well with theoretical Monte-Carlo simulations, results of which are presented in Figure 3. It is obvious from this picture, that the theoretical dependence of transmittance on sample thickness has the same decay rate as experimental curve. Distinctions of the theoretical values of transmittance of skull-scalp sample from experimental data can be explained by that average optical parameters were used in Monte-Carlo simulations.

Temperature control was provided during experiments. Temperature of the skin surface rose on 4 °C on average for the time of exposure of 4 minutes and the temperature of the external surface of the skull rose on 2 °C on average for the same time of exposure under such power of irradiation. Negligible changes of the temperature of the internal surface of the skull in few percent of degree were notice. It can be referred to inaccuracy of measurements. Dependence of temperature on time of exposure for one of the samples is represented in Table 1.
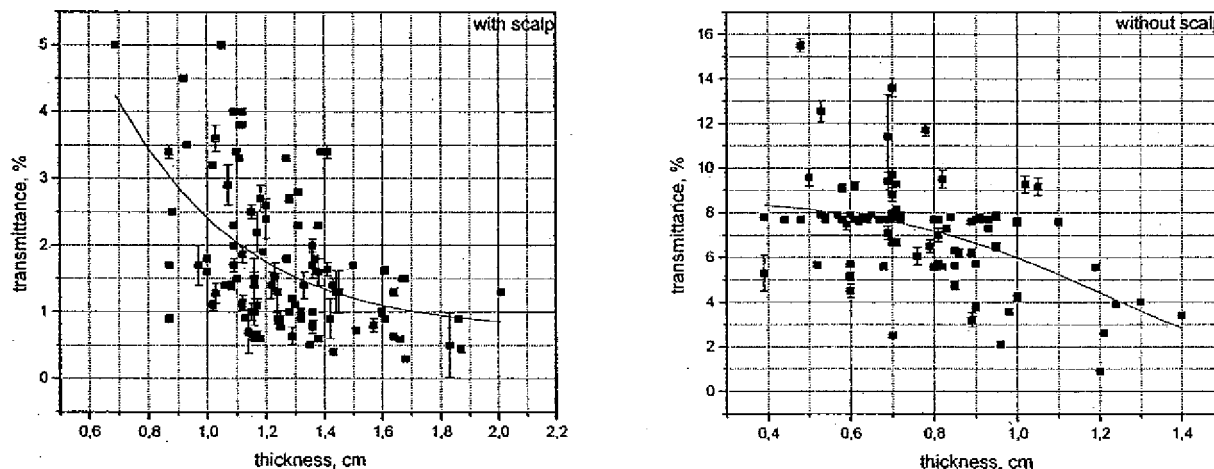


Figure 2: Dependence of transmittance on thickness of the sample – experimental results

It was said above, that the radii of equal power density (0.1, 0.5 and 0.7 of maximum value) were estimated for the distributions of power density obtained in experiments. The dependences of radius 0.5 of maximum on transmittance are presented in Figure 4. It follows from this figure, that increasing of radius 0.5maximum with increasing of transmittance is well seen in most cases. Besides that, standard deviation of each radius of fixed power density was calculated, which defined, in this case, degree of heterogeneity of tissue's transmittance related with the features of the tissue structure, mainly with the features of the bone tissue.

We can suppose that this scheme of irradiation can be used for therapeutic irradiation and can be employed for clinical study on the assumption of expected therapeutic power density at the *dura mater* of 7.5 mW/cm$^2$. Values of power density obtained in both experiment and simulation lie in this limit.
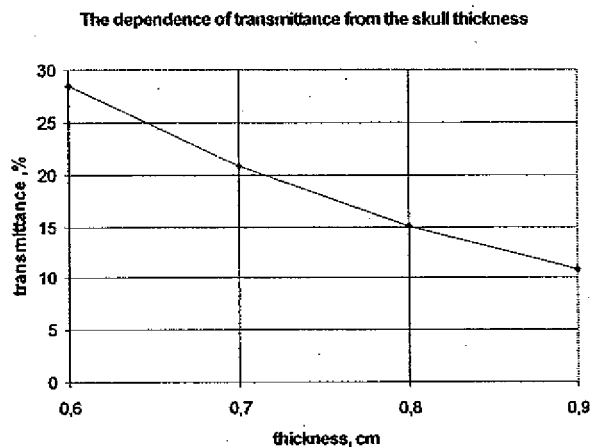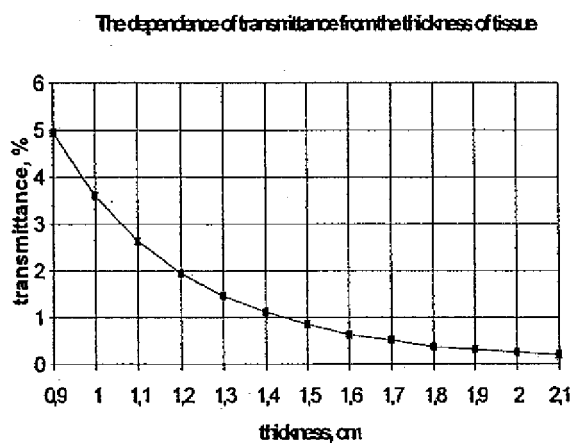
Figure 3: Dependence of transmittance on thickness of sample – Monte-Carlo simulations

| Table 1: Dependence of temperature on time of exposure | | |
|---|---|---|
| object | time of irradiation, min | temperature, °C |
| skull | 1 | 21.9 |
| scalp | 1 | 22.0 |
| skull | 2 | 22.6 |
| scalp | 2 | 23.2 |
| skull | 3 | 24.1 |
| scalp | 3 | 24.6 |
| skull | 4 | 24.8 |
| scalp | 4 | 25.6 |
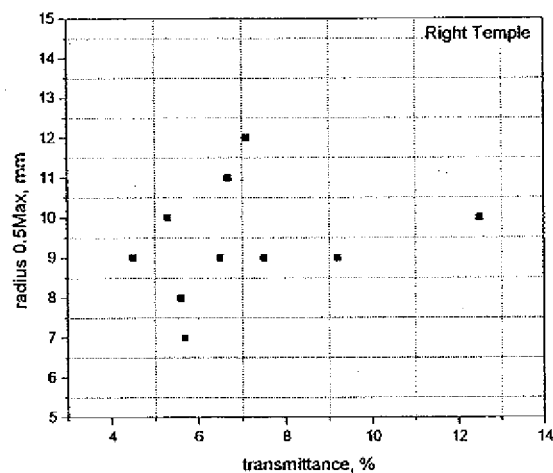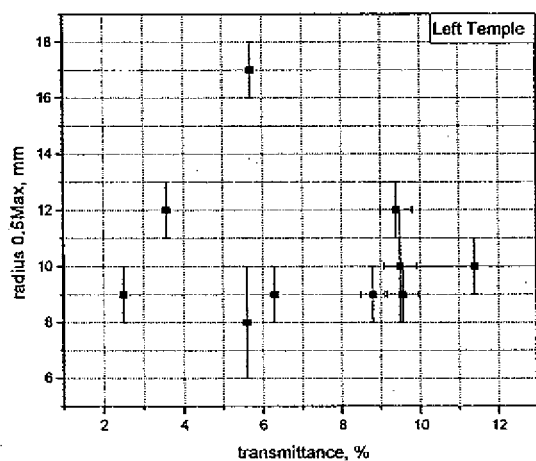


Figure 4: Dependences of radius 0.5 of maximum on transmittance

## ACKNOWLEDGEMENTS

## REFERENCES

1. Stefan Tauber, Reinhold Baumgartner, Karin Schorn, and Wolfgan Beyer, "Lightdosimetric Quantitative Analysis of the Human Petrous Bone: Experimental Study for Laser Irradiaton of the Cochlea," *Lasers in Surgey and Medicine* **28**, pp. 18-26, 2001.
2. N. Ugryumova, S.J. Matcher, D.P. Attenburrow, "Measurement of bone mineral density via light scattering," *Phys. Med. Biol.* **49**, pp. 469-483, 2004.
3. T.L. Troy, S.N. Thendnadil "Optical properties of human skin in the near infrared wavelength range of 1000 to 2200 nm," *JBO* **6**(2), pp. 167-176, 2001.
4. P.I. Begun, U.A. Shukeylo, *Biomechanics*, Politechnika, 2000, Saint-Petersburg.
5. V. V. Tuchin(Ed.), *Handbook of optical biomedical diagnostics*, SPIE Press, **PM107**, 2002, Bellingham.
6. S. Stolik, J.A. Delgado, A. Perez, L. Anasagasti "Measurements of the penetration depths of red and near infrared light in human "ex vivo" tissues" *J. of Photochemistry and Photobiology B: Biology* **57**, pp. 90-93, 2000.
7. M. Firbank, M. Hiraoka, M. Essenpreis and D.T.Delby "Measurements of optical properties of the skull in the wavelength range 650-950 nm" *Phys. Med. Biol.* **38**, pp. 503-510, 1993.

Exhibit B
Page 5 of 5